Progress in the synthesis of Al- and Cr-based sesquioxide coatings for protective applications F

Christian Martin Koller, Michael Stueber, and Paul-Heinz Mayrhofer

COLLECTIONS

Paper published as part of the special topic on Festschrift Honoring Dr. Steve Rossnagel

F   This paper was selected as Featured

View Online   Export Citation   CrossMark

ARTICLES YOU MAY BE INTERESTED IN

Progress in the synthesis of Al- and Cr-based sesquioxide coatings for protective applications

Christian Martin Koller,[1,2,3,a)] Michael Stueber,[4] and Paul-Heinz Mayrhofer[1,2]

[1]*Christian Doppler Laboratory for Application Oriented Coating Development at the Institute of Materials Science and Technology, TU Wien, Getreidemarkt 9, 1060 Vienna, Austria*
[2]*Institute of Materials Science and Technology, TU Wien, Getreidemarkt 9, 1060 Vienna, Austria*
[3]*Pankl Engine Systems, Pankl Racing Systems GmbH, Kaltschmidstrasse 2-6, 8600 Bruck a.d. Mur, Austria*
[4]*Karlsruhe Institute of Technology, Institute for Applied Material IAM, Hermann-von-Helmholtz-Platz 1, 76344 Eggenstein-Leopoldshafen, Germany*

The challenge of synthesizing protective alumina coatings in corundum structure at moderate temperatures inspired the development of novel strategies of both thin film processing and microstructural thin film design. While the growth of pure corundum coatings is still a domain of chemical vapor deposition, new concepts developed in physical vapor deposition addressed the growth of advanced solid solutions, nanocomposites, or multilayers. The system Al-Cr-O has received huge attention as thin films of the type $(Al_{1-x}Cr_x)_2O_3$ could be grown at substrate temperatures even below 500 °C in laboratory model experiments. These coatings offer particular potential for applications that require chemical inertness, thermal stability, mechanical strength, and excellent tribological properties at elevated temperatures. Mastering its low temperature deposition is one of the major aims of industrial research, as it would also enable the protection of temperature-sensitive components and consequently path the way for novel, yet not realizable applications. This work summarizes the state of the art and recent progress in the development and synthesis of such sesquioxide protective coatings prepared by physical vapor deposition. General coherencies are described for $(Al_{1-x}Cr_x)_2O_3$ coatings. Topics covered are important growth parameters (i.e., the oxygen gas flow and the substrate bias), the chemical composition and its impact on alloying concepts applicable to $(Al_{1-x}Cr_x)_2O_3$ coatings, specific architectural coating designs, and relevant properties such as the thermal stability and material response upon annealing in oxidative environments. In addition, a brief outlook into the development of other Cr-based sesquioxide thin films, $(Cr,Zr)_2O_3$ and $(Cr,V)_2O_3$, is given. © 2019 Author(s). All article content, except where otherwise noted, is licensed under a Creative Commons Attribution (CC BY) license (http://creativecommons.org/licenses/by/4.0/). https://doi.org/10.1116/1.5120793

I. INTRODUCTION

The application of thin films to modify bulk surfaces in accordance with the corresponding application is anything but a novel concept.[1] Yet, in recent decades, surface engineering gained significant importance due to ecological and economic reasons. The variety of different deposition techniques ranges from relatively simple varnishing to high complex plasma-based deposition techniques such as physical vapor deposition (PVD). The latter, a fairly flexible technique with respect to applicable materials systems, is—in the field of tool or component protection—typically associated with nitrides, carbides, or borides. However, when requirements like hardness, wear resistance, or structural stability at elevated temperatures are not sufficient and coatings have to withstand chemically hazardous environments, oxides may most appropriately represent the material of choice.

Aluminum-based oxides are essentially important as bulk materials and also intensively investigated in form of thin ($<5\,\mu m$) protective coatings as they inherently demonstrate chemical inertness in most environmental conditions. Owing to these characteristics, Al_2O_3 coatings are of particular interest for cutting and tooling industry[2] or as permeation barriers.[3]

Yet, the formation of Al_2O_3 films is not straightforward, and the research is dealing with adequate technologies and material science approaches since decades. Al_2O_3 films grown by physical vapor deposition form different metastable polymorphs, strongly depending on synthesis conditions.[4–9] Among these, the thermodynamically stable α (corundum) structure is considered to exhibit the most adequate properties for protective applications under the anticipated impact of temperature—namely, a high wear resistance, electrical resistance, chemical stability, and low ion mobility.[10–12] Other metastable polymorphs such as γ (Refs. 13–15) or κ (Ref. 16) may also be grown for protective application (e.g., cutting tools) as they indicate properties of similar potential. A distinct drawback is, however, the thermally-induced transformation into α[17–22] and often their existence by PVD is inevitable due to various reasons, such as differences in the surface energy of, e.g., γ-Al_2O_3 as compared with α-Al_2O_3 (Ref. 23) or kinetic limitations.

A decisive parameter is the surface temperature T_{dep} at which these coatings are formed. Generally, the lower the T_{dep} (affected by the deposition temperature and temperature increased by ion bombardment), the higher the fine-crystalline

a)Author to whom correspondence should be addressed: christian.koller@pankl.com

or x-ray amorphous phase fraction.[24] However, also the reactive gas pressure is decisive, probably more than in other systems, as Al_2O_3 exhibits a narrow stoichiometric margin and does not form other stable oxides than the M_2O_3-type. Yet, the necessity of deposition temperatures far beyond 600 °C distinctively limits the number of applicable substrate materials and those applications, for which alumina coatings may be particularly promising, have to be omitted. Steels, for instance, might be subject to unintended tempering during deposition temperatures beyond 400 °C and demands to lower the synthesis temperature while still being able to control microstructure (and thus properties) is encouraging research activities in academia and industry.

The trend for Al_2O_3-based films from chemical vapor deposition (CVD) to PVD is omnipresent and deposition temperatures at around 600–800 °C[25,26] can nowadays be considered for industrially-scaled α-structured alumina films. Concepts promoting the PVD synthesis of crystalline Al_2O_3 films at lower temperatures include filtered cathodic arc evaporation,[24,27] plasma-assisted techniques[26,28,29] and enhanced ion bombardment,[20,27,29–32] or the application of seed layers for epitaxial growth.[33–35] The latter not only include (low temperature) deposition of Al_2O_3 onto Cr_2O_3 (Refs. 34 and 36) but also vice versa.[37,38] A multilayer coating architecture may also benefit from enhanced hardness and toughness as recently demonstrated at the example of nitride films.[39,40]

The most important and successful strategy of materials science is alloying and has for Al_2O_3 not only experimentally been investigated[41–43] but also exploited by means of computation materials science.[9,44,45] Cr, which forms the isostructural Cr_2O_3 oxide with lattice parameters only slightly larger than α-Al_2O_3 (compare ICDD patterns #00-038-1479 with #00-046-1212) can be considered the most promising candidate with respect to attainable film properties and process-related factors. Both, Al_2O_3 and Cr_2O_3 exhibit strong metal-to-oxygen bonds in the range of 507.5 ± 2.9 and 461 ± 8 kJ/mol, respectively.[46] The quasibinary phase diagram of Al_2O_3–Cr_2O_3 (Refs. 47 and 48) indicates a miscibility gap below 1200 °C, see Fig. 1; however, the rapid cooling rates taking place in PVD processes allow for the synthesis of supersaturated metastable solid solutions, enabling new strategies to synthesize thin film materials for protective and functional application.[51,52] Next to the obvious strategy of stabilizing the corundum structure during film growth, the retardation of the irreversible phase transformation from metastable phases into α-Al_2O_3 [or $(Al,Cr)_2O_3$] (beyond the anticipated application temperature) was studied.[43,53]

Alloying in industrial application is in most cases associated with the use of compound cathodes with fixed composition. The cathode microstructure, in this regard, turned out to have an important role in the cathodic arc evaporation of Al-based oxides,[54,55] which will be briefly discussed.

Many of these considerations were experimentally studied on a lab scale base, but in order to effectively transfer these to the industrial utilization of $(Al,Cr)_2O_3$, in which batch sizes are large, tolerances are narrow, and process-reliability is one of the major criteria, a broader study comprising all aspects of the deposition process must be considered necessary as to understand and in further consequence tailor properties of $(Al_{1−x}Cr_x)_2O_3$ and related sesquioxides.

II. GROWTH PARAMETER IMPLICATIONS ON THE STRUCTURAL EVOLUTION OF $(Al_{1−x}Cr_x)_2O_3$ THIN FILMS

A. O_2 partial pressure and Cr content

Knowledge about the correlation between the Cr content, the oxygen partial pressure (respectively, reactive gas flow), and the attainable coating morphology and crystal structure is fundamental in order to exploit the full capacity of protective $(Al_{1−x}Cr_x)_2O_3$ films. The challenge is, however, not only limited to applied growth conditions but also the technical equipment used,[56] thus requiring a broader consideration including all aspects of the deposition system.

Witthaut *et al.* have carried out one of the first comprehensive studies covering this topic for reactively sputtered $(Al_{1−x}Cr_x)_2O_3$ thin films, concluding that crystallinity of films increase with increasing p_{O_2} and that for lower values codeposition of Cr and $(Al_{1−x}Cr_x)_2O_3$ phases takes place.[57] Diechle *et al.*[58] carried out a laboratory-scale combinatorial study on radio frequency (r.f.) reactive magnetron sputter deposition of Al-Cr-O thin films with large variation of the composition (using so-called segmented targets). The deposition was done at 500 °C onto cemented carbide substrates. Under defined conditions of the reactive gas flow and substrate bias, nanocrystalline thin films in solid solution structure, α-$(Al_{1−x}Cr_x)_2O_3$, were grown. The authors demonstrated that the crystallinity (and as well the density) of the thin films depends on the Cr concentration. In a further study,[59] it was shown that crystalline thin films in corundum structure could be obtained even at substrate temperatures around 300 °C. However, films with high Al content grew in x-ray amorphous structures, especially at low substrate temperature (200–300 °C). Experiments carried out in laboratory scale with monolithic alloy targets (of different Al:Cr composition) confirmed the results of the combinatorial studies. All deposited films exhibited only a very small deviation from the perfect 2:3 stoichiometry. The lattice constants a and c increased with increasing Cr/(Al + Cr)-ratio.

Apart from reactively sputtered $(Al_{1−x}Cr_x)_2O_3$ films, information on the impact of growth parameters (e.g., oxygen partial pressure or cathode composition) and the evolving phase composition for the industrially highly relevant cathodic arc process is scarce.[54,60–65] Attainable film growth rates and consequently, a higher throughput make this technique inevitable for many component or automotive applications.

The correlation between the oxygen flow rate during deposition and Cr content within powder-metallurgically prepared cathodes for industrial cathodic arc evaporated $(Al_{1−x}Cr_x)_2O_3$ coatings (x = 0.75, 0.70, 0.50, and 0.25) is illustrated by grazing-incidence XRD patterns in Fig. 2. The deposition temperature is 550 °C. The metallic films were grown with 20 sccm Ar per active source (p.a.s. ~ 0.26 Pa p_{O_2}) and 50, 100, or 250 sccm O_2 p.a.s. (which roughly
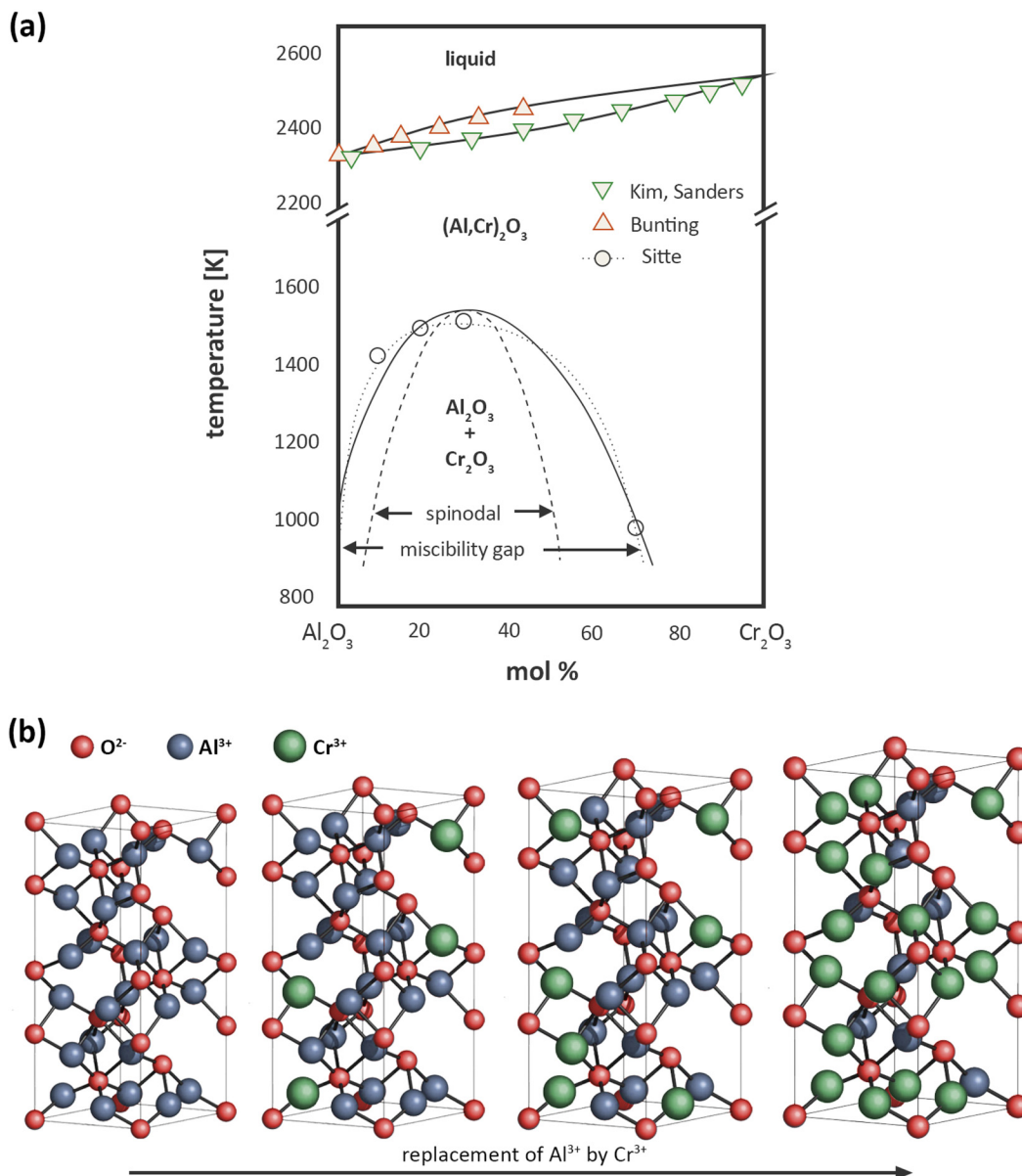
FIG. 1. Schematic lattice structure of corundum-type $(Al_{1-x}Cr_x)_2O_3$ with Cr^{3+} (large green spheres) substituting Al^{+3} (medium blue spheres) on the metallic sublattice ($^1/_3$ vacant). O^{2-} ion fully populate the nonmetal hexagonal sublattice. Adapted from Refs. 49 and 50. (a) Reprinted with permission from Kim and Sanders, J. Am. Ceram. Soc. **84**, 1881 (2001). Copyright 2019, The American Ceramic Society. (b) Reprinted with permission from Rollmann *et al.*, Phys. Rev. B Condens. Matter Mater. Phys. **69**, 165107 (2004). Copyright 2019, American Physical Society.

corresponds to 0.01–0.02 and 2 Pa O_2 deposition pressure) were used to prepare oxide coatings.

The crystallographic composition of the metallic coatings basically represents what can be anticipated from the nominal cathode compositions and the binary Al-Cr phase diagram.[68] The Al-rich coatings prepared from $Al_{0.75}Cr_{0.25}$ and $Al_{0.70}Cr_{0.30}$ cathodes consist of an intermetallic γ_2-type Al_8Cr_5 phase, whereas the Cr-rich films indicate $AlCr_2$, body-centred cubic (bcc) Cr, and/or a bcc-Cr(Al) solid solution. Introducing oxygen to the deposition (flow rate to 50 or 100 sccm O_2 p.a.s.) leads to weakening of the intermetallic XRD peaks yet without indication for oxide phases. Accordingly, the overall O_2 partial pressure (~0.02 Pa) is still insufficient to full oxidize all metallic species generated at the cathode surface. Only for the coatings prepared under oxygen-rich growth conditions (250 sccm O_2 p.a.s. ~ 2.5 Pa deposition pressure[67,69]), XRD peaks indicative for either metastable cubic[63–70] or hexagonal $(Al_{1-x}Cr_x)_2O_3$ phases are present.

As shown by Dalbauer *et al.*,[66] the coating chemistry deviates from nominal cathode composition with an Al-depletion for high Cr cathode contents and low oxygen flow rates. The closest match between cathode and coating composition is given for the coatings prepared with 100 sccm O_2 p.a.s. The maximum oxygen content of 45–58 at. % obtained by SEM-energy-dispersive x-ray spectroscopy (EDS) and elastic recoil detection analyses (ERDA) in the films prepared with 50 or 100 sccm O_2 p.a.s. is still below 60 at. %, the characteristic value for stoichiometric sesquioxides.[66]
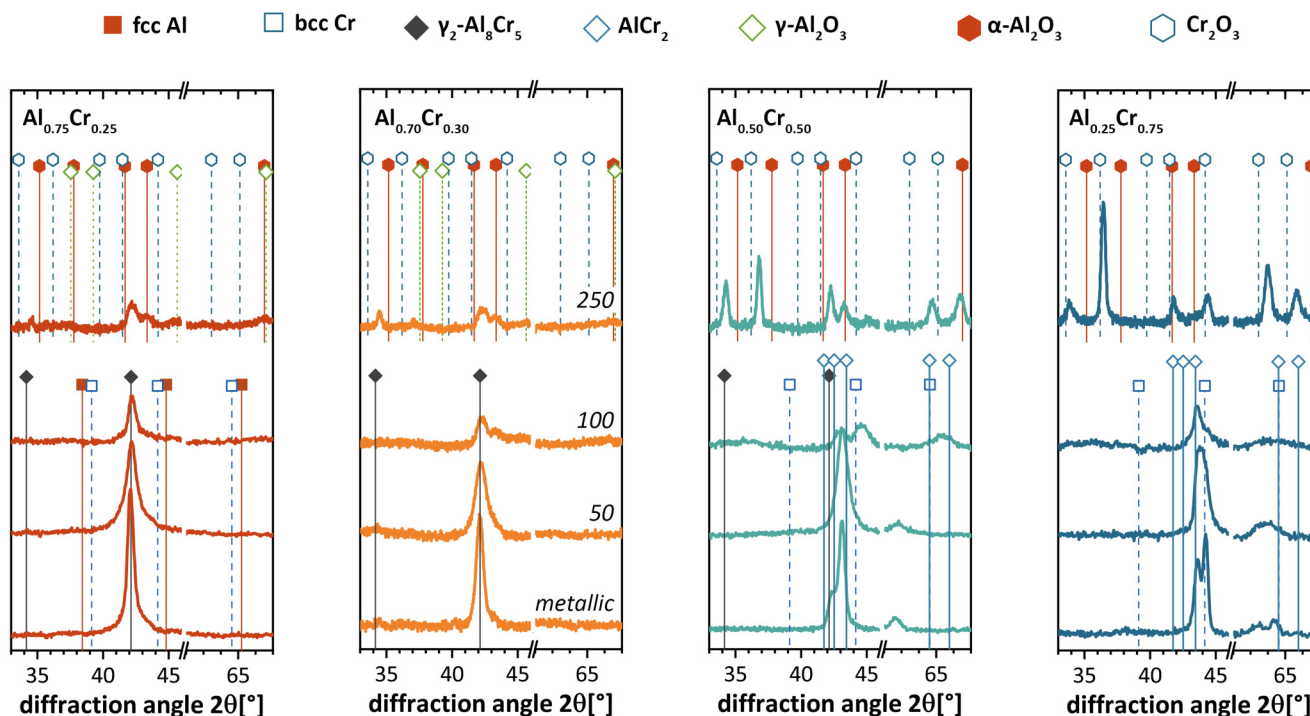
FIG. 2. GID patterns of $Al_{0.75}Cr_{0.25}$-, $Al_{0.70}Cr_{0.30}$-, $Al_{0.50}Cr_{0.50}$-, $Al_{0.25}Cr_{0.75}$-based coatings deposited in the metallic mode or either 50, 100, or 250 sccm O_2 p.a.s. on sapphire substrates. Reference ICDD data are indicated. Adapted from Refs. 66 and 67. Reprinted with permission from Dalbauer et al., Surf. Coat. Technol. **352**, 392 (2018). Copyright 2018, Elsevier. Reprinted with permission from Koller et al., Surf. Coat. Technol. **342**, 37 (2018). Copyright 2018, Elsevier.

Corresponding cross-sectional transmission electron microscopy (TEM) images with selected area electron diffraction (SAED) insets, shown in Fig. 3, corroborate XRD results, pointing out the intermetallic nature of these films. Coatings prepared in metallic mode exhibit large columns with closely-packed column boundaries. The incorporation of oxygen leads to grain refinement as the change from spot-like SAED patterns into almost continuous diffraction rings suggests. The phase composition of either γ_2-Al_8Cr_5 or $AlCr_2$, however, remains unaffected. Metallic macroparticles of various shape and size are present in all coatings and will be discussed in more detail later. Contrast differences in the form of thin lines parallel to the substrate surface are detectable in both coatings prepared with 100 sccm O_2 p.a.s. and stem from substrate rotation induced selective reactivity of Al and Cr with O.[65,71,72]

Subsequent investigations on the structure evolving by gradually increasing the O_2 partial pressure during the deposition of $Al_{1-x}Cr_xO$ (x = 0.25, 0.3, 0.5, and 0.75) coatings were performed to complement previous results and to shed further light on mechanisms taking place in the intermediate (or transition zone) from intermetallic coatings to fully stoichiometric sesquioxides.[72,73] Thereby, instead of using one fixed oxygen partial pressure during the entire deposition process, a gradual increase from 0 to 250 sccm O_2 p.a.s. was realized. Four identical cathodes were simultaneously arc evaporated. In order to link each
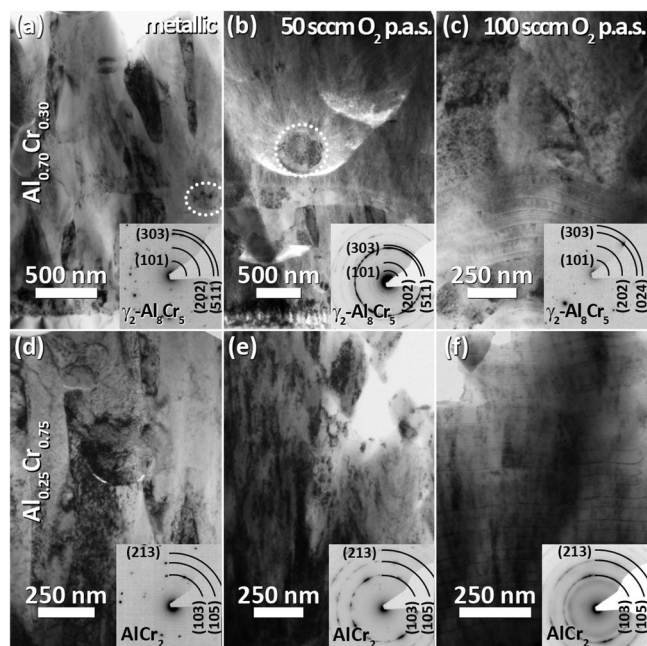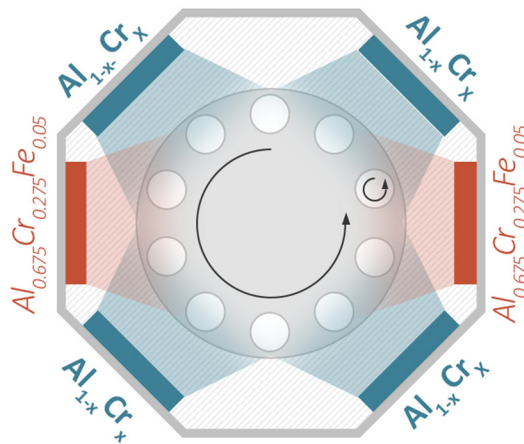

FIG. 3. Bright field TEM micrographs of our $Al_{0.70}Cr_{0.30}$- and $Al_{0.25}Cr_{0.75}$-based coatings with corresponding SAED patterns. Incorporated defects are highlighted by dotted white circles and ellipses. (a)–(c) represent the micrographs for the $Al_{0.70}Cr_{0.30}$-based coatings and (d)–(f) show the $Al_{0.25}Cr_{0.75}$-based coatings. Adapted from Ref. 66. Reprinted with permission from Dalbauer et al., Surf. Coat. Technol. **352**, 392 (2018). Copyright 2018, Elsevier.

coating section to a specific gas flow rate (consider the nonlinear film growth taking place with linear increasing oxygen flow rate), an Fe-containing ($Al_{0.675}Cr_{0.25}Fe_{0.05}$) tracer layer was grown every 50 sccm O_2 p.a.s. With two additional cathodes being simultaneously evaporated together with four $Al_{1-x}Cr_x$ cathodes, the oxygen flow present within the tracer layer consequently decreased, which is important to bear mind when interpreting TEM results.
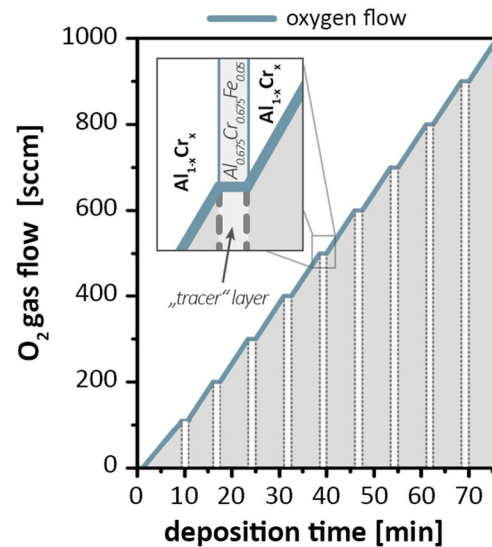
X-ray nanodiffraction studies combined with cross-sectional SEM images of $Al_{0.75}Cr_{0.25}$ and $Al_{0.25}Cr_{0.75}$-based coatings prepared with an oxygen gradient, shown in Fig. 4, illustrate the structural evolution as a function of the oxygen gas flow and the Cr cathode content. Up to approximately 4.5 μm, the $Al_{0.75}Cr_{0.25}$-based film exhibits a noncolumnar almost featureless cross-section dominated by an intermetallic γ_2-Al_8Cr_5 phase (see the dark blue diffraction at around 42°). A broader signal at around 45° 2θ appears beginning
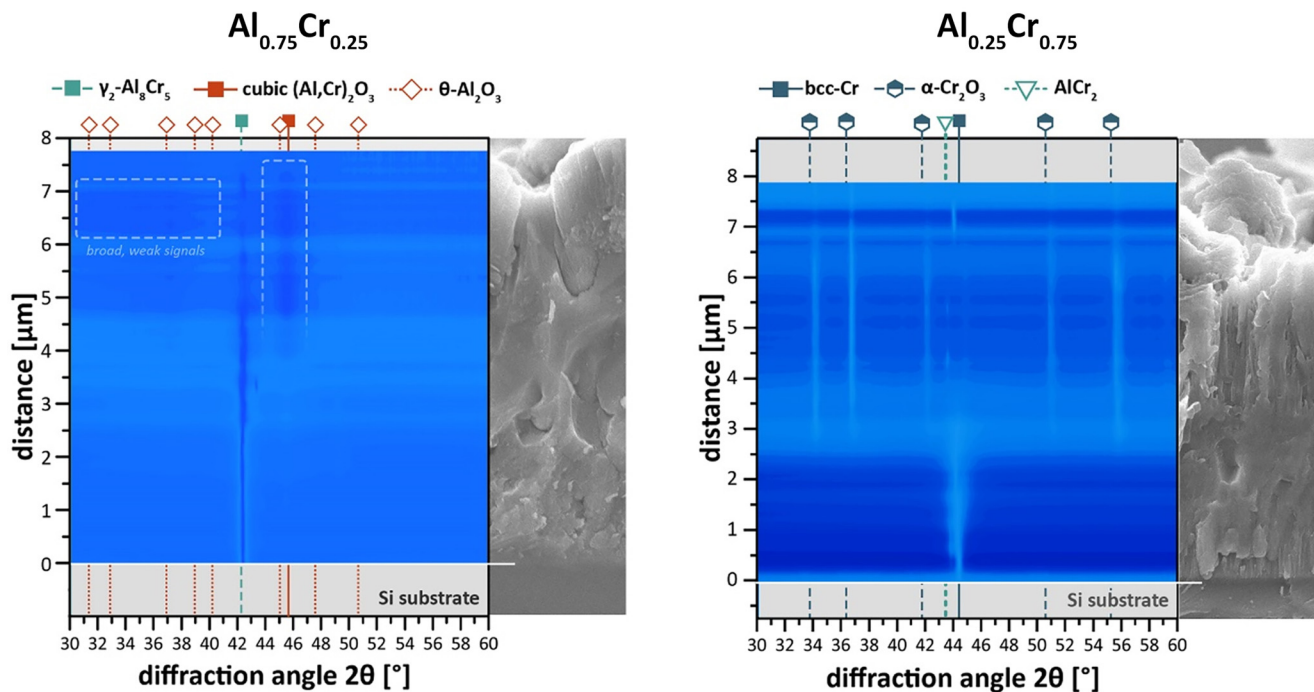

FIG. 4. (a) Deposition set-up and reactive gas flow management for $(Al_{1-x}Cr_x)_2O_3$ coatings prepared with an oxygen gradient. (b) Combined x-ray nanodiffraction and cross-section SEM studies of $Al_{0.75}Cr_{0.25}$- and $Al_{0.25}Cr_{0.75}$-based $(Al,Cr)_2O_3$ coatings prepared with an oxygen gradient.

with $\sim 4.5 \mu m$ coating thickness and simultaneously the growth morphology becomes fine-fibrous. Additional weak diffraction peaks appear beginning with $6 \mu m$ coating thickness. The uppermost coating section, hence, where a maximum oxygen flow rate of 250 sccm O_2 p.a.s. was used, still exhibits a strong intermetallic and metastable cubic character. Diffraction peaks of hexagonal phases are not present.

Contrarily, the $Al_{0.25}Cr_{0.75}$ coating—also showing a featureless intermetallic dominated (Cr and $AlCr_2$) morphology in the low-O_2 regime close to the substrate—crystallizes in a hexagonal solid solution already beginning with approximately $3 \mu m$ film thickness. The corresponding diffraction peaks excellently agree with a calculated $(Al_{0.25}Cr_{0.75})_2O_3$ solid solution. The fracture cross-section of the upper coating section shows pronounced columnar features.

Details on the growth morphology between the intermetallic coating section and the transition regime at the example of $Al_{0.70}Cr_{0.30}$- and $Al_{0.25}Cr_{0.25}$-based coatings are given by cross-section TEM studies Figs. 5 and 6, respectively.[72,74]

The coating section of the $Al_{0.70}Cr_{0.30}$-based film close to the substrate very well agrees with that of the monolithically grown films showing a compact large-grained intermetallic microstructure. With already 35 sccm O_2 p.a.s. [Fig. 5(c)], the columnar growth is hindered and bright appearing grain boundaries in growth direction are forming. With approximately 60 O_2 p.a.s., the columnar growth is entirely interrupted and a randomly-oriented globular microstructure with grain sizes in the range of 10–15 nm develops. Elongated crystallites (~ 25 nm oriented in growth direction) form with ~ 70 sccm O_2 p.a.s., which are separated by thin layers perpendicular to the substrate surface. Further increasing the oxygen flow rate to ~ 90 sccm O_2 p.a.s. leads to even finer structures consisting of small crystallites (dark contrasted) embedded in a bright matrix, see Fig. 5(f). According to SAED, scanning transmission electron microscopy (STEM)-EDS, and electron energy loss spectroscopy (EELS) investigations, the globular crystallites are enriched in Cr, whereas the surrounding material exhibits higher Al and O contents. The Fe-containing tracer layer is partially shown in the bottom of Fig. 5(g). Here, as the O_2 flow rate per active source is locally reduced, the microstructure again resembles that of the ~ 70 sccm O_2 p.a.s. regime and after stopping the two $Al_{0.675}Cr_{0.275}Fe_{0.05}$ tracer cathodes, again shows fine globular features. Indication for stoichiometric $(Al_{1-x}Cr_x)_2O_3$ phases is not given for oxygen flow rates below ~ 125 sccm O_2 p.a.s. Beyond, fine-grained metastable cubic phases nucleate. The uppermost coating section, where the oxygen gas flow is increased to the maximum value of 250 sccm O_2 p.a.s., is still dominated by the metastable cubic structure, although locally a small fraction of hexagonal phases can be detected.

The structural evolution of the $Al_{0.25}Cr_{0.75}$-based coating prepared with an oxygen gradient is summarized in Fig. 6, by combining TEM BF, scanning transmission electron microscopy (STEM), energy-dispersive x-ray spectroscopy (EDS), and combined high resolution (HR) TEM SAED images. The Fe-containing tracer layers can well be distinguished by contrast differences in the TEM BF and STEM images as well as the EDS line scan. The corresponding HR TEM images [Fig. 6(c)] show that the microstructural modifications generally resemble those of the $Al_{0.70}Cr_{0.30}$ film triggering grain refinement and interruption of columnar growth initiated by the introduction of oxygen to the growth process. However, the fraction of fine-structured almost amorphous boundary phases in-between the crystalline areas is reduced, and already with 110–125 sccm O_2 p.a.s., the nucleation of V-shaped hexagonal-structured crystallites is observed. It is worth to note that some of these apparently originate from the horizontally-aligned crystalline layers [Fig. 6(f), indicated by dashed white lines]. This could indicate a preferential nucleation on Cr-rich crystallites. Yet, more in-depth investigations are necessary to shed light on this observation, and if a partial oxidation of these particles to Cr_2O_3 took place, it led to locally preferred nucleation sites for the α phase. However, based on these results, we can conclude that the transition regime between intermetallic structures to a fully stoichiometric coating is with 110–125 sccm O_2 p.a.s. relatively similar for both $Al_{0.70}Cr_{0.30}$ and $Al_{0.25}Cr_{0.75}$-based coatings. Nonetheless, the Cr content distinctively influences whether crystalline columnar hexagonal or extremely fine-crystalline almost amorphous metastable cubic phases evolve.
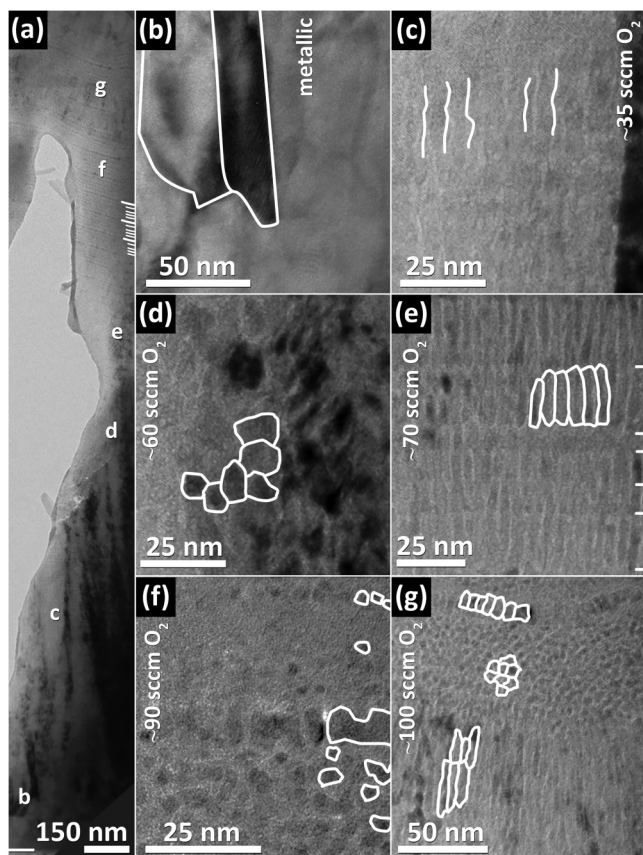

FIG. 5. TEM cross-section image of an $Al_{0.70}Cr_{0.30}$ coating prepared with an oxygen gradient showing the transition regime to full stoichiometric sesquioxides. Adapted from Ref. 72. Reprinted with permission from Koller *et al.*, Scr. Mater. **139**, 144 (2017). Copyright 2017, Elsevier.
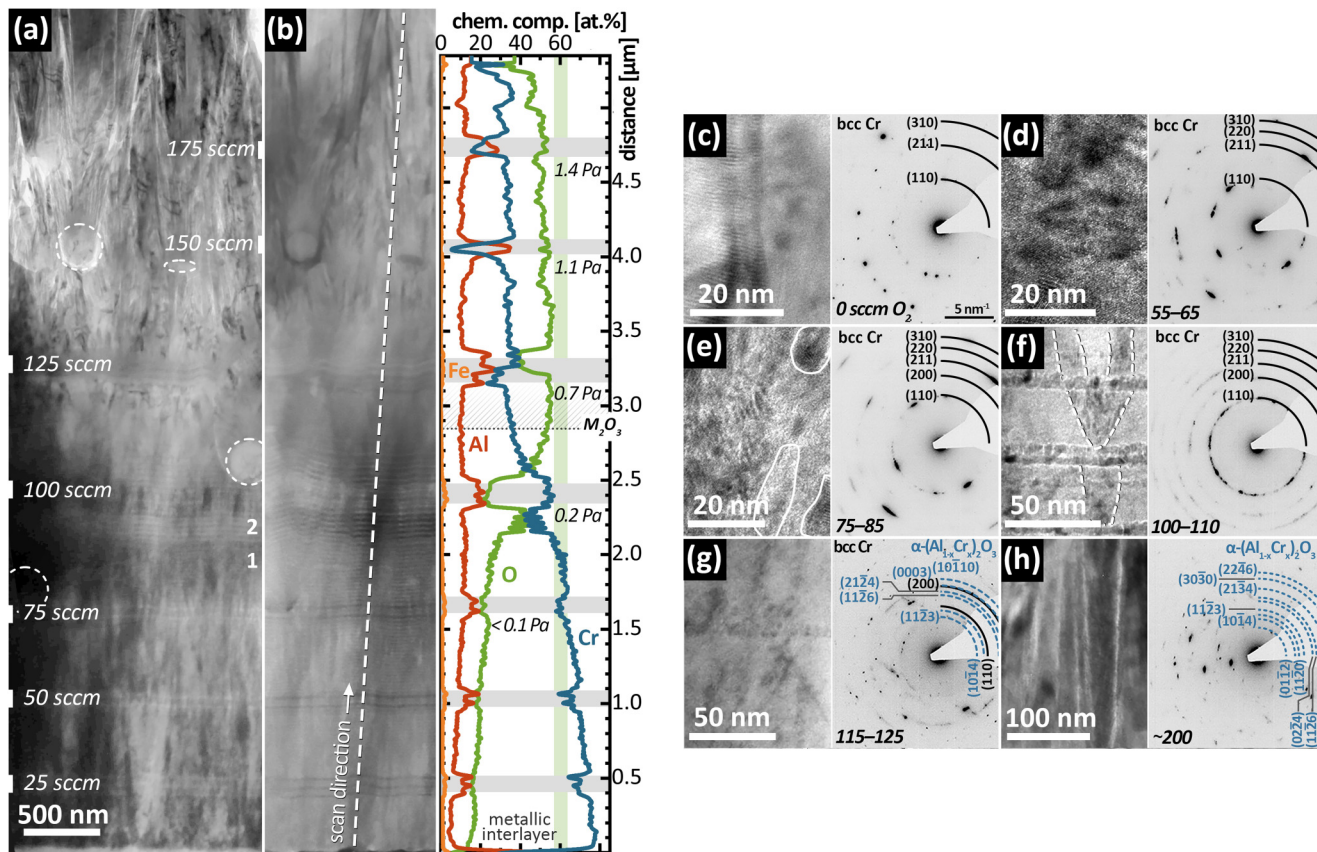
FIG. 6. Cross-sectional TEM image of the $Al_{0.25}Cr_{0.75}$-based coating grown with an oxygen gradient. Adapted from Ref. 74. Reprinted with permission from Koller *et al.*, Vacuum **155**, 645 (2018). Copyright 2018, Elsevier.

These findings excellently agree with the observation of a codeposition of Cr and Al_2O_3 by Witthaut *et al.* for reactively sputtered films under oxygen-depleted growth conditions[57] and indicate that in the arc evaporation process of $Al_{1-x}Cr_x$ compound cathodes, Al preferentially bonds with O, forming a boundary phase between yet not oxidized metallic or intermetallic crystallites of Cr. Only for oxygen flow rates sufficient to fully react with all metallic species reaching the substrate surfaces crystalline $(Al_{1-x}Cr_x)_2O_3$ solid solutions nucleate and no metallic or intermetallic domains form. For the Al-rich compositions $Al_{0.75}Cr_{0.25}$ and $Al_{0.70}Cr_{0.30}$ fine-crystalline metastable cubic phases form, which subsequently turn into a mixed cubic and hexagonal phase composition with progressing film thickness. Chromium contents of more than 50 at. % in the cathodes, on the other hand, initially promote the crystallization of a hexagonal solid solution for the given deposition parameters. As soon as growth conditions change, e.g., reduction of the O_2 gas flow below the threshold value for stoichiometric sesquioxides, the microstructure is governed by selective oxidation of the most oxygen affine element present.

X-ray diffractograms of monolithically grown $(Al_{1-x}Cr_x)_2O_3$ films (250 sccm O_2 p.a.s.) on different substrate materials are shown in Fig. 7. Both Al-rich coatings ($Al_{0.75}Cr_{0.25}$ and $Al_{0.70}Cr_{0.30}$) crystallize in a dual phase structure consisting of metastable cubic and hexagonal solid solutions. Thereby, the substrate material does influence the XRD peak shape but not the phase composition itself. The initial growth stage

is in both cases dominated by a fine-crystalline metastable cubic fraction, from which with progressing film thickness corundum-type solid solutions evolve. The calculated lattice parameters of the hexagonal solid solution indicate a close match with a linearlike Vegard's behavior[75] and increases with higher Cr content in the films.
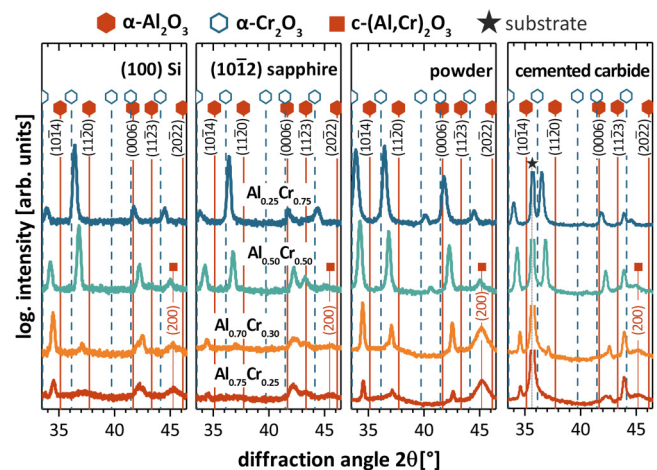
FIG. 7. XRD patterns of $(Al_{1-x}Cr_x)_2O_3$ coatings prepared from $Al_{0.75}Cr_{0.25}$, $Al_{0.70}Cr_{0.30}$, $Al_{0.50}Cr_{0.50}$, and $Al_{0.25}Cr_{0.75}$ cathodes, deposited on different substrate materials and in powdered state. Adapted from Ref. 67. Reprinted with permission from Koller *et al.*, Surf. Coat. Technol. **342**, 37 (2018). Copyright 2018, Elsevier.

The lattice parameter a_{cub} of the metastable cubic $(Al_{1-x}Cr_x)_2O_3$ phase also slightly varies with the chemical composition as the comparison with Khatibi et al.,[70,76] Najafi et al.,[63] and Diechle et al.[58] shows. It is smallest for the Al-rich and largest for the Cr-rich compositions.

High resolution TEM images of the hexagonal solid solution and metastable cubic phase are compared in Fig. 8. Hexagonal crystallites are generally pronounced V-shaped, whereas the cubic solid solution can rather be described as fine-grained or even fibrous and shows a predominant random growth orientation. Accordingly, differences in specific properties such as the diffusion barrier capabilities can be anticipated.[64]

B. Cathode modifications

Physical vapor deposition techniques such as reactive sputter deposition and cathodic arc evaporation, in general, allow for a great flexibility in the selection of target (referred to in the context of sputter deposition) and cathode (CAE) materials. Multicomponent coatings such as $(Al_{1-x}Cr_x)_2O_3$ may be grown either by codeposition using pure Al or Cr target/cathodes or by the use of dedicated Al-Cr compounds, see Fig. 9(a). A major advantage of the former method is the possibility to adjust the chemical composition of the films by varying the target/cathode power settings (and to some extent with the help of the reactive gas flow). Yet, for industrial application, where process stability and constant quality levels are of utmost importance, compound cathodes with a fixed nominal composition may be more convenient. Coatings in

this article were to the most part synthesized by powder-metallurgically produced $Al_{1-x}Cr_x$ compound cathodes.

The cathode state during arc evaporation is essential for the process stability and coating quality.[54] During the discharge and the timeframe of deposition, the surface near cathode material undergoes distinct modifications. The arc spot locally evaporates and heats the material to such an extent that a molten pool of cathode elements forms in which elements intermix and subsequently solidify. It was shown by various authors that the nature of the so-called cathode reaction zone and its coverage by intermetallic or ceramic (if the process gas incorporates) compounds depends on the cathode microstructure as well as the reactive gas and total process pressure.[54,55,77,78] Consequently, also the ion charge state distribution is affected.[79,80] It is shown that Cr^+ ions are dominant for p_{O_2} of around 1×10^{-3}–1×10^{-4} Torr, whereas a higher fraction of Cr^{++} or Cr^{+++} ions is observed at pressure levels lower than 1×10^{-6} Torr. For Al cathodes, a similar observation is made, yet with Al^+ and Al^{++} fractions prevailing at lower pressure values than 1×10^{-4} Torr, and Al^+ being dominant $>1 \times 10^{-4}$ Torr.

The highest number of macroparticles incorporated into $(Al,Cr)_2O_3$ films occurs for the largest fraction on low-melting phases at the cathode surface. If higher melting, intermetallic compounds form, a significant reduction of droplets takes place. This is also the reason for the particular importance of $(Al,Cr)_2O_3$ thin films for the cathodic arc evaporation process, as pure Al cathodes with its enhanced droplet generation and instable process conditions are considered not be applicable from an industrial consideration, even with magnetic filter systems.[81,82] Yet, the formation of nonconductive oxide pillars also depends on the cathode composition as the comparison of different $Al_{1-x}Cr_x$ cathodes in Fig. 9(c) demonstrates (please bear in mind that slight differences in the average grain size are also given). Important in this regard is also the cathode microstructure, namely the Al and Cr grain size. For each cathode composition, an ideal grain size leading to complete intermixing and thus homogeneous evaporation can be expected, which, however, is also strongly related to the process gas flow as Fig. 10 shows. The x-ray diffractograms of the cathode surface after arc evaporation indicate differences related to the grain size (small 2FK, larger FK, and large GK). Specifically for the larger grain distribution in cathodes and a higher O_2 flow rate, XRD peaks indicative for free Al are clearly visible. Accordingly, the droplet generation and subsequent incorporation into the coatings is more likely. Comparing the cross-sectional SEM images in Figs. 10(b) and 10(c) clearly reveal differences between reaction zone of large and fine-grained $Al_{0.70}Cr_{0.30}$ cathodes. The former exhibits free Al at the surface (dark gray areas), whereas the thin bright appearing intermetallic phase (cracks indicate its brittleness) covers the entire cathode surface for the fine-grained cathode.

Not only the Al and Cr distribution in the cathodes can be used to influence the formation of nonconductive oxide pillars on the cathode surface but also the alloying of dedicated elements such as Si (Ref. 83) or B (Ref. 84) can effectively increase process stability.

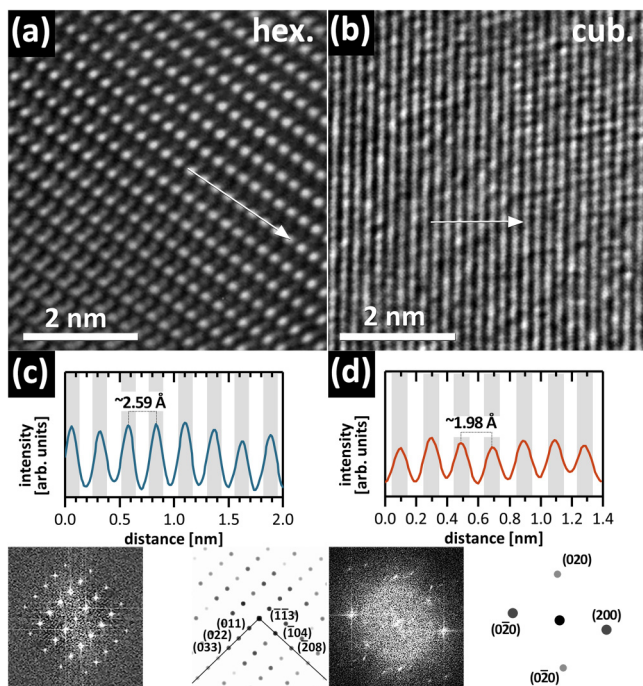FIG. 8. HR TEM images of (a) a hexagonal and (b) metastable cubic $(Al_{1-x}Cr_x)_2O_3$ film prepared from $Al_{0.75}Cr_{0.25}$ cathodes. Adapted from Ref. 67. Reprinted with permission from Koller et al., Surf. Coat. Technol. **342**, 37 (2018). Copyright 2018, Elsevier.
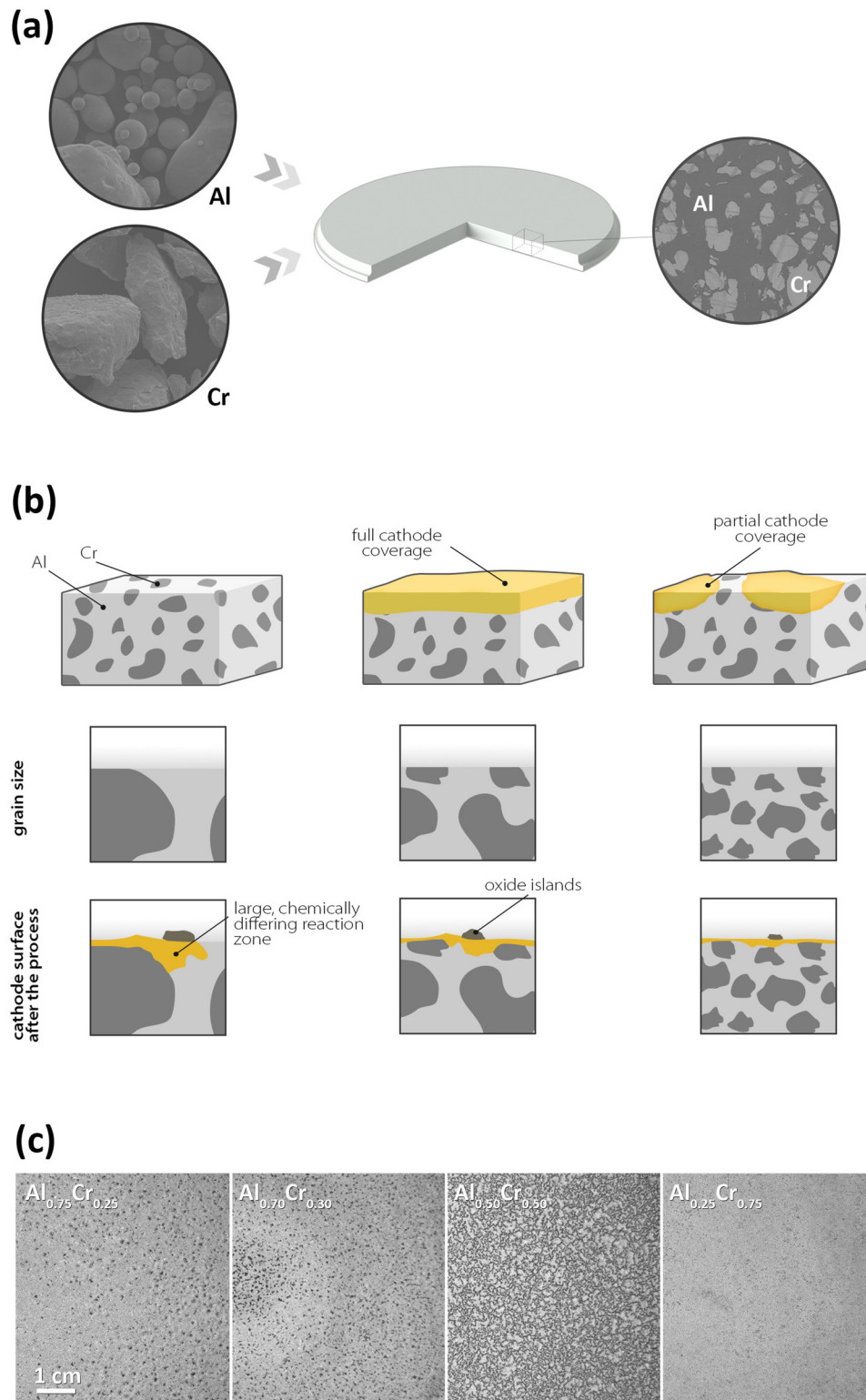
FIG. 9. (a) SEM overview images of Al and Cr powders used for the Al-Cr compound cathodes, schematically shown and with a surface SEM image. (b) Schematic illustration of the cathode surface coverage for three different grain sizes, after the cathodic arc evaporation process in O_2 atmosphere. (c) Photographs of different $Al_{1-x}Cr_x$ cathode surfaces showing different "poisoning states" after the cathodic arc evaporation with $p_{O_2} = 2.5$ Pa (oxygen-rich growth conditions).

C. Alloying elements

The effect of dopants on the structural stability of α over metastable phases such as θ or γ has intensively been addressed by density functional theory (DFT) calculations for pure Al_2O_3. According to Wallin et al., B, Cr, Co, Mo, and W improve the stability of the θ-Al_2O_3 phase, whereas Cu stabilizes α-Al_2O_3.[45] Jiang et al.[85] investigated the impact of Cr, Si, Sc, Ti, and Y on the relative stability
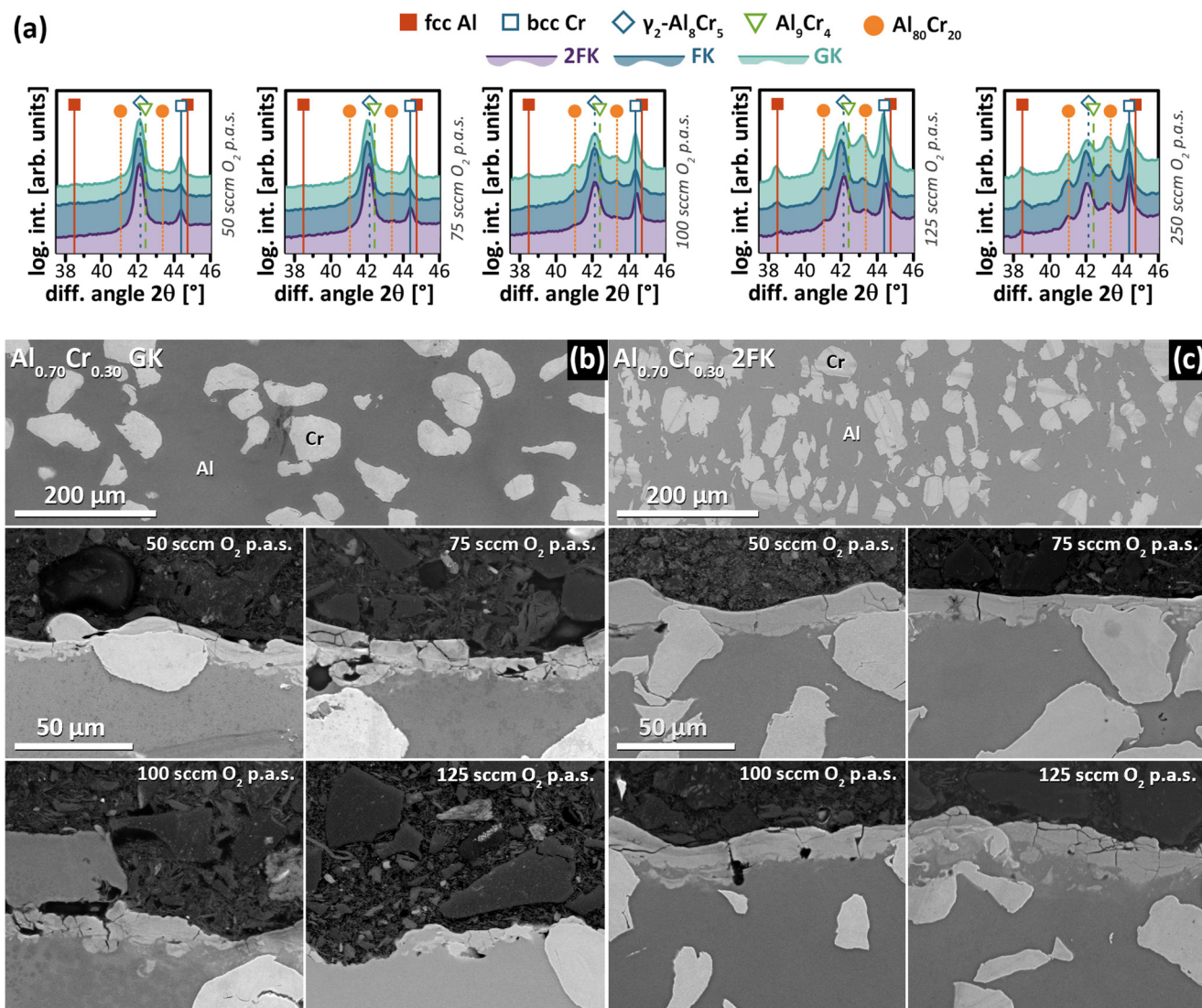
FIG. 10. X-ray diffractograms of $Al_{0.70}Cr_{0.30}$ cathode surfaces with different Al and Cr grain sizes, arc evaporated with 50, 75, 100, 125 or 250 sccm O_2 p.a.s. (b) and (c) show cross-section SEM images of large (GK) and smaller (2FK) grain-sized cathodes for different O_2 gas flow rates.

(by comparing the energies of formation E_f) of two different γ-Al_2O_3 modifications (spinel and Hausmannite) with α-Al_2O_3. Sc, Y, and, especially, Si decrease the energy of formation for γ-Al_2O_3, whereas Cr acts destabilizing in both cases—thus favoring α-Al_2O_3. Ti, on the other hand, increases E_f for the spinel type and decreases E_f within Hausmannite γ-Al_2O_3. The discrepancy between theoretical prediction and actual experimental observations, especially for Cr, may, on the one hand, be attributed to kinetics that prevail thermodynamics, and on the other hand, on impurities and point defect generations of the deposition process itself.[47,86–88] These may be of extrinsic nature like residual water vapor or hydrogen or of intrinsic nature such as built-in defects (vacancies, interstitials, etc.). Hydrogen is essentially one element that drastically influences the properties of alumina-based coatings. Schneider et al. have calculated the impact of H additions on the binding energy of α-Al_2O_3, clearly showing a distinct decrease from 9.31 to 8.32 eV/atom at 6.6 at. %.[30]

Studies on cathodic arc evaporated $(Al_{1-x}Cr_x)_2O_3$ coatings alloyed with small amounts of Fe were initiated by idea that Fe, which also forms a hexagonal sesquioxide Fe_2O_3 with lattice parameters slightly larger than those of Cr_2O_3 and forming solid solutions with Al_2O_3 and Cr_2O_3 at elevated temperatures,[89] may improve the α-stabilizing effect of Cr in Al_2O_3.[69] The combination of these elements results in improved oxidation resistance in various bulk materials by forming a dense and stable oxide scale upon high temperature exposure in ambient atmosphere,[90,91] giving rise to also follow this concept for thin film development. Another indication of a beneficial effect to Fe can be found in the observations made by Mühlbacher et al.[92] revealing that small quantities of Fe in $Al_{1-x}Cr_x$ cathodes favor the formation of Cr_2O_3 during oxidation of $Al_{1-x}Cr_xN$ coatings prepared.

Interestingly, the apparent increase of α phase fraction in Fe-alloyed $Al_{0.70}Cr_{0.30}$-based $(Al,Cr)_2O_3$ coatings prepared by cathodic arc evaporation is not exclusively based on the formation of a $(Al,Cr,Fe)_2O_3$ solid solution, rather the

incorporation of small particles emerging from the cathode surface (referred to as droplets or macroparticles) seem to influence the phase formation,[93,94] Figs. 11(a)–11(d). However, not all macroparticle types favor the hexagonal structure. Specifically those with a high Al content and large size (i.e., ≥ 150 nm) may also negatively affect the film growth. The nucleation onto these structures leads, as can be seen from Fig. 11(e), to renucleation of fine-grained cubic structures. The effect of larger (either spherical or flat-shaped) droplets becomes even more evident when looking at a top-view prepared $(Al_{0.675}Cr_{0.275}Fe_{0.05})_2O_3$ TEM sample, see Fig. 11(f). The large dark-appearing Cr-rich droplet (lower right) leads to severely distorted film growth in its vicinity and interrupts columnar growth of the mixed hexagonal/cubic film, see the left part of the image.

So, in order to make use of macroparticles in terms of triggering of a hexagonal solid solution, very specific droplet shapes and sizes (in addition to the droplet chemistry) have to be present. This makes it rather difficult to intentionally create this effect and a technical utilization is on a larger scale yet not feasible.

A summary of the structural modifications of various alloying elements in cathodic arc evaporated $(Al_{1-x}Cr_x)_2O_3$ coatings processed in oxygen-rich atmosphere is given by cross-sectional TEM images in Fig. 12. The $Al_{0.70}Cr_{0.30}$-based coating [Fig. 12(a)] indicates a dual phase composition of a fine-grained and thin-columnar cubic phase with the occasional presence of V-shaped hexagonal crystallites. The latter dominate the Cr-rich coating [Fig. 12(b)] morphology with partially underdense column boundaries. Adding Fe, as previously shown, increases the hexagonal phase fraction [Fig. 12(c)],
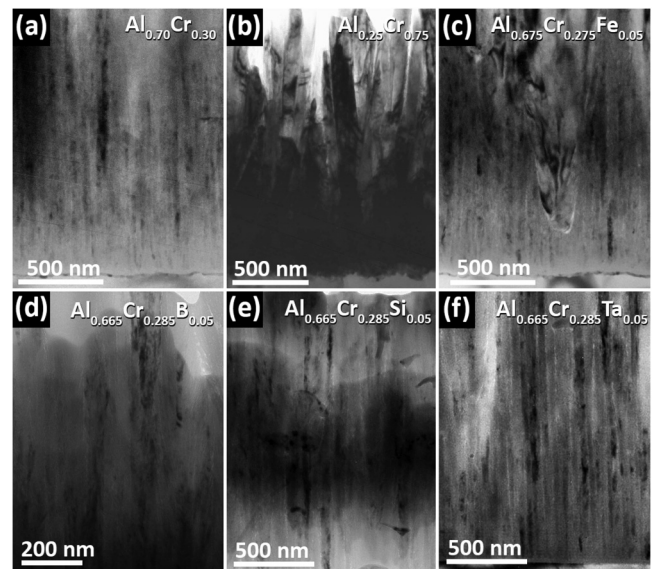

FIG. 12. Cross-sectional TEM BF images of various $(Al_{1-x}Cr_x)_2O_3$ coatings prepared by cathodic arc evaporation under comparable growth conditions. Differences originating from the Cr content [compare (a) and (b)] as well as the impact of 5 at. % of (c) Fe, (d) B, (e) Si, or (f) Ta.

whereas B [Fig. 12(d)] and Si [Fig. 12(e)] further decrease the grain size of the cubic phase and supress the formation of corundum-type crystallites. Additionally, a higher number of smaller droplets appear to be incorporated into the film. Pronounced underdense column boundaries are observed for the $Al_{0.665}Cr_{0.285}Ta_{0.05}$-based coating, Fig. 12(f). According to x-ray diffraction analyses (not shown), the coating is predominately cubic-structured with indications of other, yet not identified phases.

D. Bias potential

Modifying the coatings' microstructure and stress state by ion bombardment is one essential benefit of PVD techniques as numerous examples show.[95–102] By applying a high negative potential to the substrate holder positively charged ions get accelerated and contribute to the film growth on impact. For electrically conducive films such as CrN or TiN a DC bias potential setting may be convenient, yet electrically nonconductive films require a more sophisticated set-up to prevent from charge buildup and therewith associated time-dependent degradation of coating quality. Typically, pulsed or RF bias settings are applied when growing Al-Cr-O films. One of the most recent studies on this topic, specifically focused on $(Al_{1-x}Cr_x)_2O_3$ films, was carried out by Pohler et al., who show that the α phase fraction can be effectively adjusted by optimizing the pulsed bias duty cycle $\eta = t_{neg}/(t_{neg} + t_{pos})$[61] (Fig. 13). η values of 70%, 90%, and 95% lead to well-developed $(Al_{1-x}Cr_x)_2O_3$ solid solutions ($Al_{0.50}Cr_{0.50}$ cathodes used) with minor fractions of a metastable cubic phase (see the diffraction peaks at ~45° and 66° 2θ), whereas η = 100% significantly decreases the crystalline α fraction. An optimum (highest α and lowest metastable cubic XRD peaks) is given for a duty cycle of 95%.
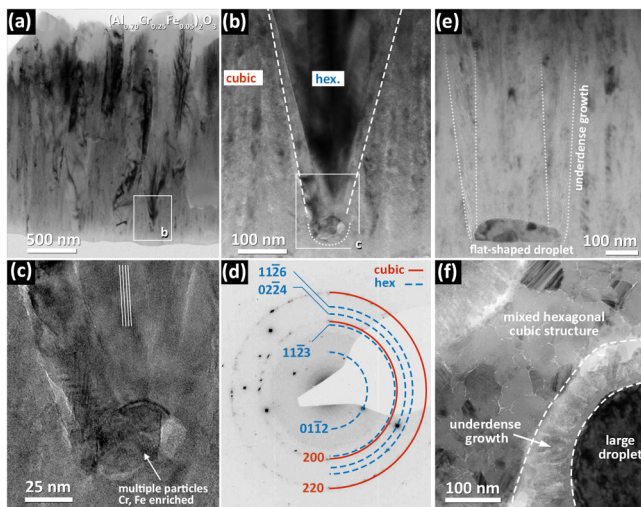

FIG. 11. (a)–(d) Cross-sectional TEM studies revealing the existence of small macroparticles acting as nuclei for α-structured phases in Fe-alloyed $Al_{0.70}Cr_{0.30}$-based $(Al,Cr)_2O_3$ coatings prepared by cathodic arc evaporation. (e) shows the negative influences of smaller flat-shaped droplets on the subsequent film growth. (f) represents a top-view TEM image where a large spherical-shaped droplet leads to significant undersense coating in its vicinity. Adapted from Refs. 93 and 94. (a)–(f) Reprinted with permission from Koller et al., Surf. Coat. Technol. **276**, 735 (2015). Copyright 2019, Springer Nature. Reprinted with permission from Koller et al., BHM Berg-Hüttenmänn. Monatsh. **161**, 325 (2016). Copyright 2015, Elsevier.
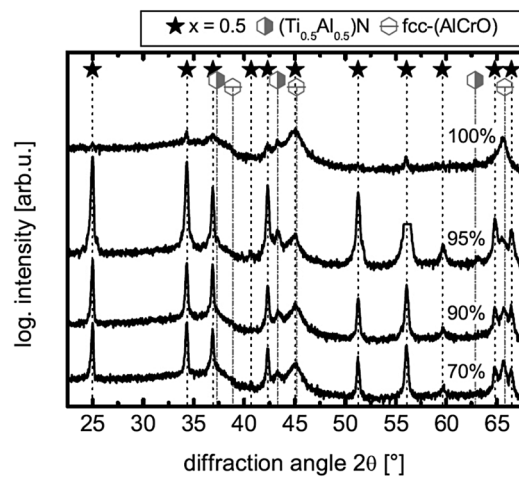
FIG. 13. Impact of the pulsed bias duty-cylce $\eta = t_{neg}/(t_{neg} + t_{pos})$ (70%, 90%, 95%, or 100%) on the structural evolution of $(Al_{0.50}Cr_{0.50})_2O_3$ coatings prepared by cathodic arc evaporation. Adapted from Ref. 61. Reprinted with permission from Pohler et al., Surf. Coat. Technol. **282**, 43 (2015). Copyright 2015, Elsevier.

As previously shown, alloying $(Al_{0.70}Cr_{0.30})_2O_3$ coatings with Fe is an effective way to shift the phase composition towards the corundum-type solid solution. Accompanied with this is a slight increase of hardness and indentation modulus, see Fig. 14(a). Higher pulsed bias values during film growth increases both H and E as can be seen from
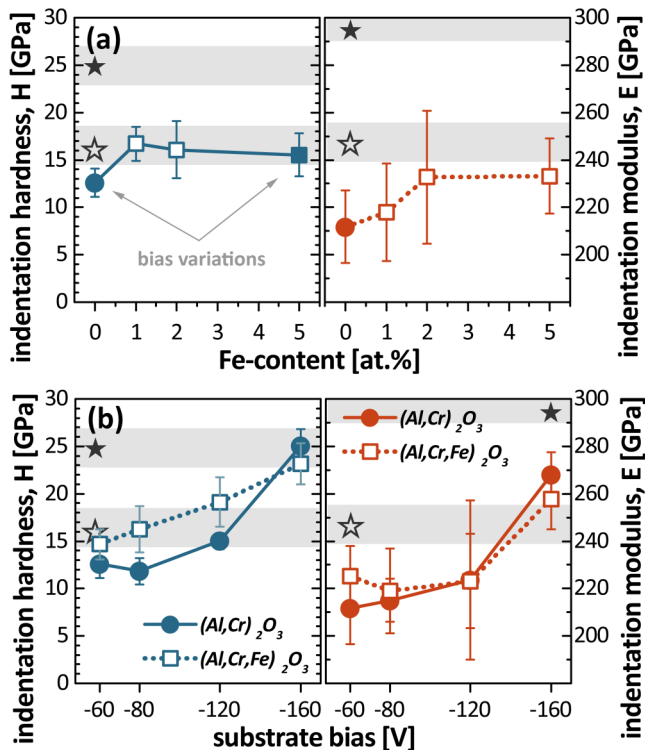

FIG. 14. Hardness and indentation moduli of cathodic arc evaporated $(Al_{0.70}Cr_{0.30})_2O_3$-based coatings on Si substrates as a function of the Fe content (a) and substrate bias (b). Adapted from Ref. 103. Reprinted with permission from Koller et al., Surf. Coat. Technol. **319**, 386 (2017). Copyright 2017, Elsevier.

Fig. 14(b). Thereby, the hardness difference originating from Fe-alloying increases for intermediate bias values and vanishes for the maximum bias value of −160 V. The indentation moduli instead, basically follow the same trend, independent on the alloying element.

The structural evolution associated with an increased pulsed substrate bias is revealed by XRD investigations (Fig. 15), showing that the phase composition for a fixed η value seems to be relatively constant, whereas the growth orientation of the hexagonal phase continuously changes. The ability to influence the texture is of significance, as the example of CVD-prepared α-Al_2O_3 films show. The best wear resistance was obtained for a growth orientation with (0001) planes oriented parallel to the tool surface.[104] Both coatings, the Fe-free and Fe-alloyed one, still exhibit a pronounced metastable cubic phase fraction as can be seen from the XRD peaks at $2\theta \sim 45°$ and $66°$.

E. Coating architecture

Many protective coating systems are composed of several (repetitive) layers rather than just consisting of one chemically and structurally constant layer. The simplest approach can be an adhesion layer to compensate for differences between coating and substrate, which may negatively affect the coating efficiency. Such an architecture is, for instance, of utmost importance for highly loaded diamondlike carbon (DLC) films used for automotive applications.[105] Apart from that, aiming for enhanced mechanical properties is often the reason for a more complex coating architecture. With respect to Al_2O_3 thin films, researchers also often follow the idea of stabilizing the corundum structure by epitaxial growth on dedicated seed layers. Particularly, the isostructural Cr_2O_3 represents an ideal candidate capable of triggering the nucleation of α-Al_2O_3 during reactive sputter deposition at temperatures as low as 280 °C.[106,107] Density function theory calculations suggest that due to low relaxations and surface
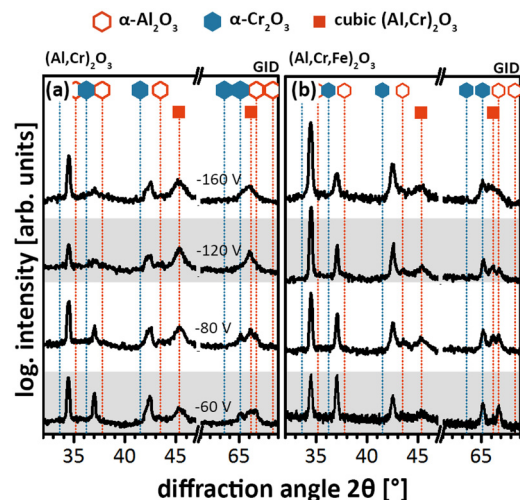

FIG. 15. Grazing-incidence X-ray diffraction (GID) study of $(Al_{0.70}Cr_{0.30})_2O_3$ and $(Al_{0.675}Cr_{0.275}Fe_{0.05})_2O_3$ coatings as a function of the pulsed substrate bias voltage. Adapted from Ref. 103. Reprinted with permission from Koller et al., Surf. Coat. Technol. **319**, 386 (2017). Copyright 2017, Elsevier.
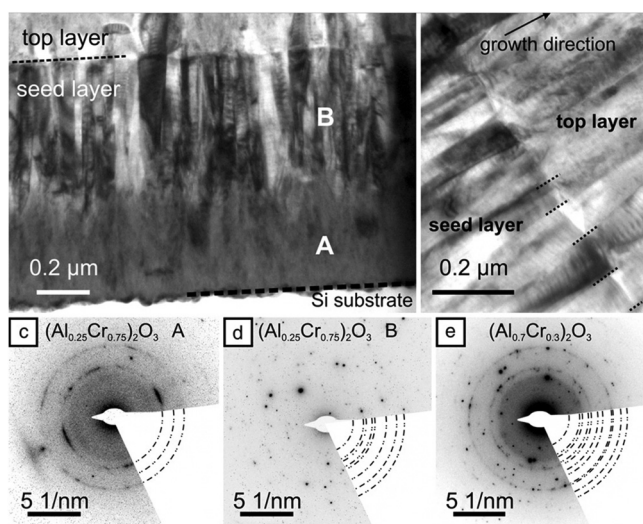
FIG. 16. Cross-sectional TEM (a) overview image and (b) detail of the top layer/seed layer interface. The corresponding SAED patterns of the $(Al_{0.25}Cr_{0.75})_2O_3$ seed layer with regions A and B and the $(Al_{0.70}Cr_{0.30})_2O_3$ top layer (all prepared by CAE) are presented in (c)–(e), respectively. Adapted from Ref. 109. Reprinted with permission from Pohler et al., Thin Solid Films **550**, 95 (2014). Copyright 2014, Elsevier.

energy, the α-Cr_2O_3 $(10\bar{1}2)$ lattice plane is the preferred one for local epitaxial growth of α-Al_2O_3.[108]

The first study on cathodic arc evaporated Al-rich $(Al_{1-x}Cr_x)_2O_3$ layers deposited onto Cr-rich $(Al_{1-x}Cr_x)_2O_3$ seed layers using an industrial deposition plant was carried out by Pohler and co-workers[109] showing that by such a concept, Al-rich films with $x = 0.85$ and 0.70 can be grown in the corundum structure—which is not possible (in a single-phased nature) by a monolithic deposition process. As can be seen from Fig. 16, columns of the dark-appearing Cr-rich hexagonally-structured phases extend into the bright appearing Al-rich oxide film. SAED patterns taken at different positions corroborate the structural stabilization, only with slight variations in the lattice parameters due to the changed chemistry. Overcoming the initial nucleation of the

seed layer was reported to be detrimental for the effectiveness of transferring the crystal- and microstructure to the subsequent layer. Furthermore, by modifying the seed layer orientation (through substrate biasing) also the top layer can be textured. Nonetheless, the application of an interlayer or seed layer before the actual protective coating requires a certain capacity in available sources and may (also from an economical point of view) not always be feasible.

Subsequently, more complex microstructures were established in a multilayer arrangement including also quasiternary sesquioxides with Fe, Si, or B additions. XRD patterns of monolithically grown $(Al,Cr)_2O_3$, $(Al,Cr,Fe)_2O_3$, $(Al,Cr,Si)_2O_3$, and $(Al,Cr,B)_2O_3$ films on sapphire substrates are shown in Fig. 17(a), next to those of corresponding multilayers [using thin $(Cr,Al)_2O_3$ seed layers]. The multilayer architecture was realized through a twofold substrate rotation and specific cathode arrangement. Two neighboring $Cr_{0.75}Al_{0.25}$ and four $Al_{0.70}Cr_{0.30}$, $Al_{0.675}Cr_{0.275}Fe_{0.05}$, $Al_{0.665}Cr_{0.285}Si_{0.05}$, or $Al_{0.665}Cr_{0.285}B_{0.05}$ cathodes were simultaneously arc evaporated with the individual layer thickness determined by the rotation frequency (1.67 rotations per minute, bilayer period $\Lambda = 60\,nm$). The Al-rich $(Al,Cr)_2O_3$ and $(Al,Cr,Fe)_2O_3$ coatings indicate a dual phase composition consisting of a hexagonal solid solution and a finer-grained metastable cubic fraction, which by this multilayer arrangement turns into an almost single-phase hexagonal structure. The difference is even more pronounced for the Si and B alloyed film, which as monolayers, are almost x-ray amorphous. Figure 17(b) shows a schematic of their overall growth morphology, when prepared without or with a multilayer arrangement with $Cr_{0.75}Al_{0.25}$-based seed layers.

More detailed TEM investigations reveal that these films still contain a significant metastable cubic phase fraction close to the substrate, which with progressing film thickness turns into a pronounced columnar morphology [comparable to that known for Cr_2O_3 or Cr-rich $(Al_{1-x}Cr_x)_2O_3$ films].

As Figs. 18(a) and 18(b) reveal, the dominant hexagonal solid solution in these multilayers does not necessarily also imply enhanced mechanical properties. Accountable for the
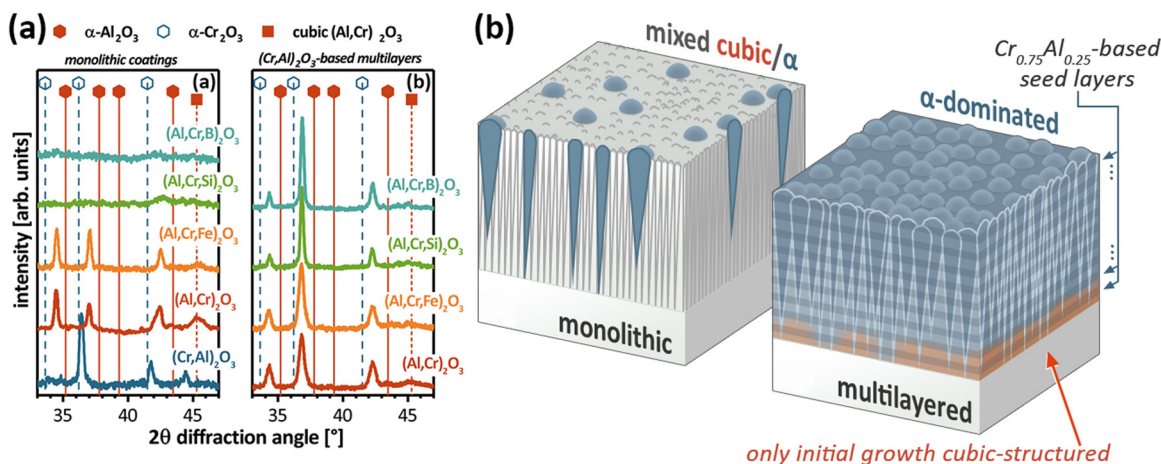

FIG. 17. (a) XRD patterns of monolithically grown $(Al_{1-x}Cr_x)_2O_3$-based films and their multilayer arrangement with thin $(Cr_{0.75}Al_{0.25})_2O_3$ layers. (b) schematic of their overall growth morphology. Adapted from Ref. 110. Reprinted with permission from Koller et al., Scr. Mater. **146**, 208 (2018). Copyright 2018, Elsevier.
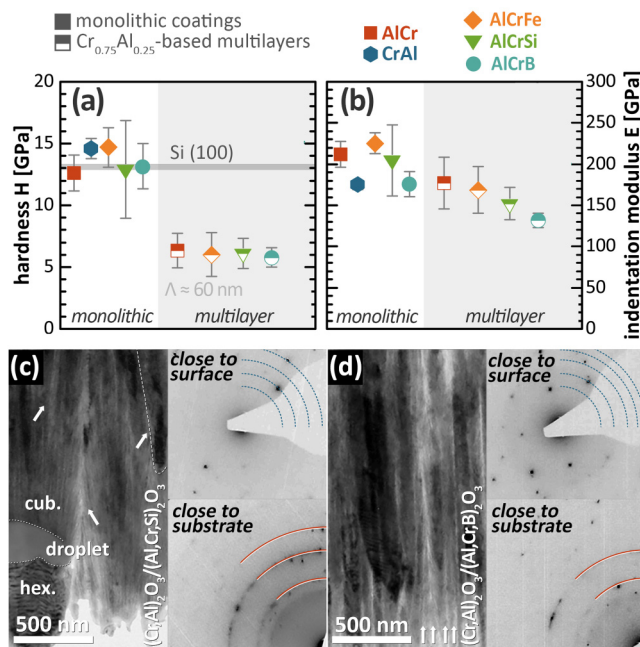
FIG. 18. (a) Hardness and (b) indentation modulus of various $(Al_{1-x}Cr_x)_2O_3$ coatings and multilayers containing $(Cr_{0.75}Al_{0.25})_2O_3$ seed layers (bilayer period of approximately 60 nm). (c) and (d) cross-sectional TEM images with corresponding SAED patterns of the Si- and B-containing multilayers, respectively. Adapted from Ref. 110. Reprinted with permission from Koller *et al.*, Scr. Mater. **146**, 208 (2018). Copyright 2018, Elsevier.

lower hardness compared to the monolithically-grown films are most likely the weaker boundaries between the large columns and/or underdense interfacial areas, see Figs. 18(c) and 18(d), respectively. Also, the incorporation of droplets [such as the flat-shaped Al-rich one shown in Fig. 18(c)] negatively influence the subsequent film growth and hence the coating's mechanical performance. In which way, such coatings perform upon thermal exposure is yet not investigated.

Another multilayer concept includes the alternating arrangement of $(Al,Cr)_2O_3$ and $(Al,Cr)N$ layers with differently-structured interfaces.[111] DSC/TGA analyses of powdered coating material revealed a retarded dissociation from CrN into Cr_2N and further Cr, and thus an improvement of the structural stability at high temperatures. Thereby, the interface geometry (gradual transition from oxide to nitride or sharp interfaces) further influences the thermally-induced decomposition.

III. THERMAL STABILITY AND OXIDATION RESISTANCE

The ability of a coating to withstand thermal load is one of the most crucial demands posed when being used as protection on the tool or component surface. However, the term thermal stability not only implies that a coating is capable of bearing 800, 1000, or even 1200 °C for a longer period of time, without suffering from oxidation or mechanical degradation alone. As mentioned in Secs. II A–II E, Al_2O_3- and $(Al,Cr)_2O_3$-based coatings exist in different polymorphic structures. Whether these occur in thin film deposition

depends on the deposition technique, the growth conditions, alloys, or impurities. In PVD-based methods such as reactive putter deposition or reactive cathodic arc evaporation, the typical phase fractions occurring in monolithically-grown Al-rich $(Al_{1-x}Cr_x)_2O_3$ films without epitaxial stabilization are either of amorphous type or gamma, respectively, B1-like.[57,60,67,70,112] Already at annealing temperatures exceeding the growth temperature, a distinct change in crystallography takes place via defect annihilation and grain coarsening of the finer structured metastable areas.

However, the only thermodynamically stable phase in Al_2O_3 is the corundum structure and for $(Al_{1-x}Cr_x)_2O_3$ solid solutions, spinodal decomposition is considered to be extremely slow,[89] as compared, for instance, with $Ti_{1-x}Al_xN$ thin films.[113,114] Therefore, coatings partially containing fractions of amorphous or metastable phases are subject to thermally-induced phase transitions, as shown in Fig. 19 for $Al_{0.75}Cr_{0.25}$-, $Al_{0.70}Cr_{0.30}$-, $Al_{0.50}Cr_{0.50}$-, and $Al_{0.25}Cr_{0.75}$-based monolithically-grown oxide coatings. Associated with this transformation are changes in the volume which consequently enables the hazard of crack generation.[115] These crack networks significantly reduce the performance of the coating and can, in worst case, result in spallation and subsequent failure of the component coated.

Researchers follow two strategies in circumventing this issue. The first and most obvious one is the formation of the thermodynamically stable phase in the as-deposited state. However, if the anticipated application temperature is limited to be in the transformation regime between metastable cubic and hexagonal phases, one could aim for chemical variations or alloying of the coating to retard the transformation to slightly higher temperatures. Examples of the former have intensively been discussed by means of the $Al_{1-x}Cr_x$ cathode composition and oxygen process flow as well as growth conditions, such as substrate biasing.

Although Al-based oxides are per definition resistant against further oxidation (provided they crystallize in the thermodynamically stable form and stoichiometric composition), extrinsic defects like droplets may still be susceptible to oxidation. The impact of alloying elements can be either favorable (presumably those forming sesquioxides) or detrimental (non-M_2O_3 oxides).

One example of defect-triggered oxidation deeper into a coating is given by Fig. 20, where Fig. 20(a) shows the left-half of the cross-section in TEM BF mode and Fig. 20(b) the right-half in STEM mode. An intermetallic Al-Cr-Fe coating was oxidized at 900 °C for 3 h. Although the formation of a thin mixed oxide scale (metastable θ-type phase) on top of the coarsened intermetallic [γ_2-$Al_8(Cr,Fe)_5$] film apparently protects the majority underneath, favorable conditions for diffusion along grain boundaries or larger three-dimensional defect surfaces become essential. A thin metastable oxide scale forms along growth defects, originating from an intermetallic droplet and thus open the possibility of local oxidation deep into the coating and thus local weakening of the film [see the dark gray-appearing Al-rich oxide scale in Fig. 20(b)].

Details on the phase transition of the metastable cubic phase fractions taking place in Al-rich $(Al,Cr)_2O_3$ films are
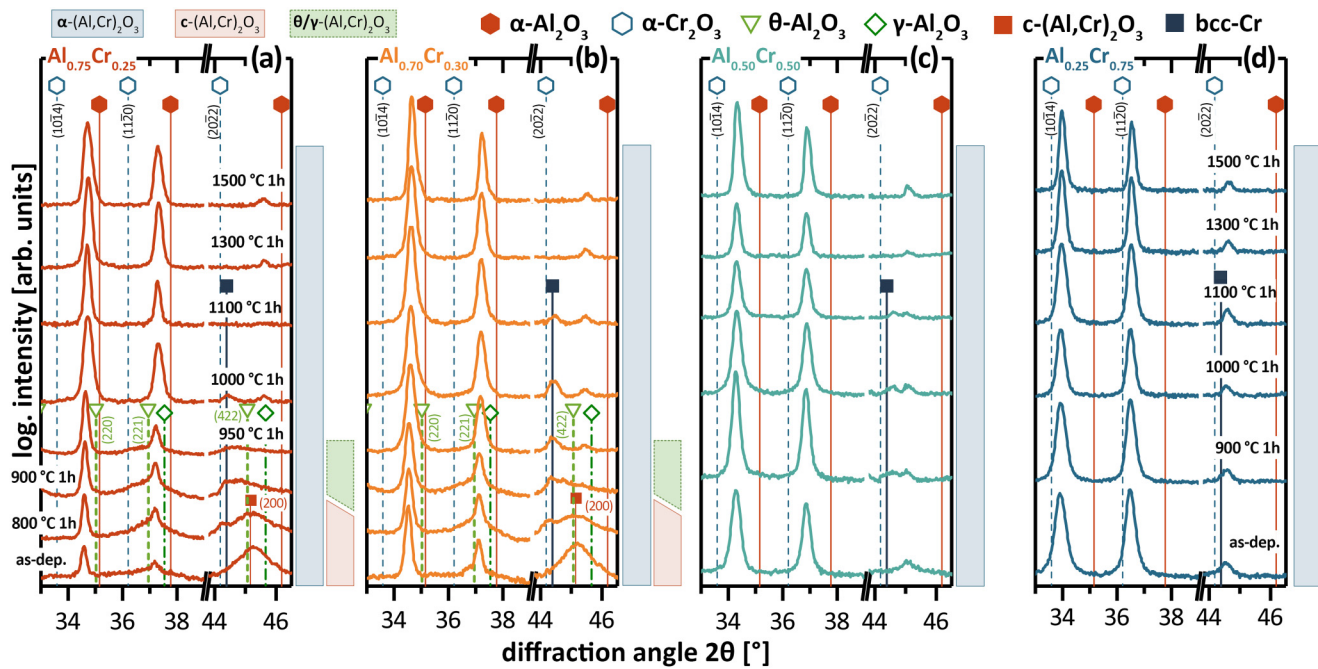
FIG. 19. Structural evolution of powdered $(Al_{1-x}Cr_x)_2O_3$ with different Cr contents during vacuum annealing treatments up to 1500 °C. Adapted from Ref. 67. Reprinted with permission from Koller et al., Surf. Coat. Technol. **342**, 37 (2018). Copyright 2018, Elsevier.

presented in the powder XRD pattern (Fig. 21). The area at around 66° 2θ covers the metastable cubic (220) XRD peak as well as those of a hexagonal $(Al_{1-x}Cr_x)_2O_3$ solid solution. The $Al_{0.75}Cr_{0.25}$-based film (left XRD patterns) exhibits one broad diffraction peak indicative of the metastable cubic phase. After annealing at 800, 900, 950, and 1000 °C for 1 h in vacuum, the XRD peak shifts to higher diffraction angles and additional weak XRD peaks develop at around 950 °C. These, as the diffraction pattern after annealing at 1000 °C shows, match a hexagonal $(Al_{1-x}Cr_x)_2O_3$ solid solution.

A slightly higher Cr content within the coating ($Al_{0.70}Cr_{0.30}$ cathodes used) leads to similar phase transition, although hexagonal XRD peaks are clearly visible already after annealing at 950 °C. Also, a slight shift to higher diffraction angles can be observed. Accordingly, the metastable phase fractions apparently phase transform into the hexagonal phase between 900 and 1000 °C—depending on the initial Cr content.

Cross-sectional TEM studies of the $Al_{0.75}Cr_{0.25}$-based film after oxidation at 900 °C, Fig. 22, show the progressing phase transformation of the fine-grained metastable cubic structure into the larger-crystalline hexagonal solid solution from the substrate-film interface. The interface between
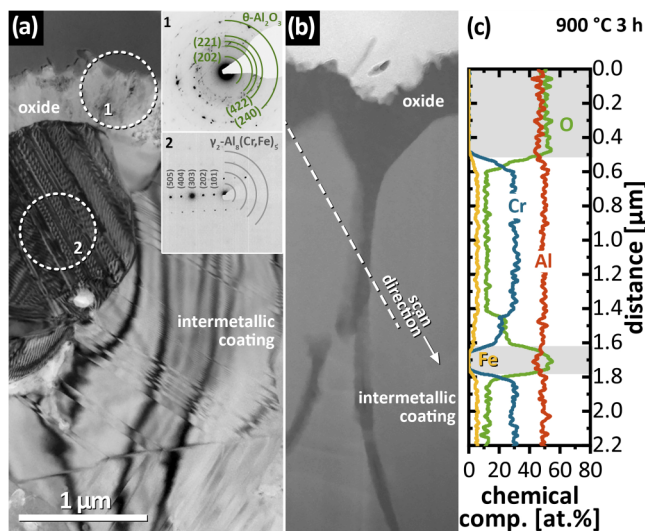
FIG. 20. Cross-sectional TEM image of an intermetallic $Al_{0.675}Cr_{0.275}Fe_{0.05}$ coating after oxidation at 900 °C for 3 h. Adapted from Ref. 116. Reprinted with permission from Koller et al., J. Vac. Sci. Technol. A **37**, 041504. Copyright 2019, American Vacuum Society.

FIG. 21. Details of the $Al_{0.75}Cr_{0.25}$ and $Al_{0.70}Cr_{0.30}$-based coatings after vacuum annealing at different temperatures showing the progressing phase transformation of metastable cubic fractions into a hexagonal solid solution. Adapted from Ref. 67. Reprinted with permission from Koller et al., Surf. Coat. Technol. **342**, 37 (2018). Copyright 2018, Elsevier.

FIG. 22. TEM images of the thermally-induced phase transformation from the metastable cubic structure into the hexagonal solid 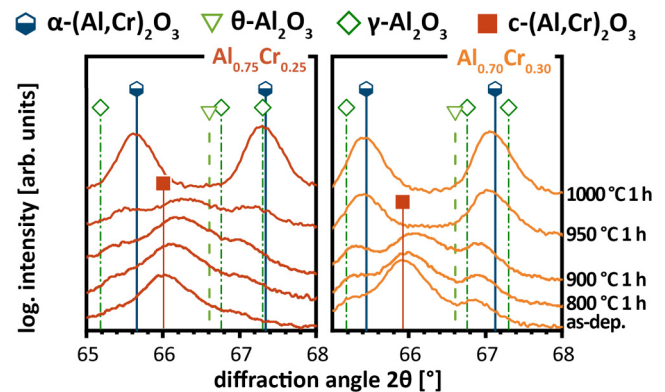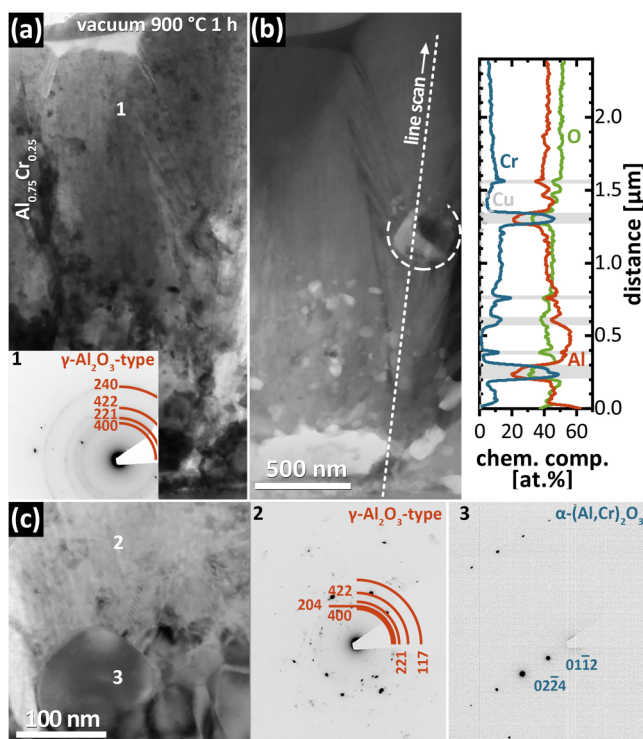solution beginning from the substrate-film interface. Adapted from Ref. 67. Reprinted with permission from Koller et al., Surf. Coat. Technol. **342**, 37 (2018). Copyright 2018, Elsevier.

the cubic and α phase is shown in the TEM BF image (c). The Z-contrast STEM image (b) also reveals the presence of an intermetallic Cr-rich droplet, which decomposes as a result of the vacuum annealing treatment.

The impact of alloying elements on the thermal stability of Al_2O_3 thin films has been investigated by several research groups in the past. For instance, Nahif et al. showed that Si additions up to 0.7 at. % within filtered cathodic arc evaporated γ-Al_2O_3 thin films effectively increase the stability range of γ and θ phases by more than 200 °C and the subsequent formation of α-Al_2O_3 by 200 °C.[43] The authors explain this observation by the formation of SiO_2 at grain boundaries, rather than the incorporation of Si into Al_2O_3 alone (see Fig. 23 for a schematic illustration).

Similarly, Bolvardi et al. have studied the impact of Si on reactively sputtered Al_2O_3 films using a combinatorial approach.[42] While the presence of SiO_2 at the grain boundaries is attributed to the increased phase transformation temperature into α-Al_2O_3, a changed bonding state is given as main explanation for the increased stability of amorphous Si-doped Al_2O_3 films. Stronger and shorter Si–O bonds replace Al–O bonds and so shift the transformation temperature by more than 100 °C.

To which extent B and Si additions influence the phase transformation sequence in Al-rich $(Al,Cr)_2O_3$ films is illustrated by powder x-ray diffraction patterns after vacuum annealing, see Fig. 24. The $Al_{0.70}Cr_{0.30}$-based reference film, Fig. 24(a), initially crystallizes in a mixed structure of metastable cubic and hexagonal phases, which upon vacuum annealing phase transform into corundum-type solid solutions between 800 and 900 °C. Smaller XRD peaks emerging between 950 and 900 °C indicate the transient formation of γ- and or θ-type phases. The B-containing film, Fig. 24(b), initially cubic dominated and fine-crystalline, shows a slightly retarded phase transition to 950 °C, whereby longer annealing times have a similar effect on the structural evolution as higher temperatures (see the patterns annealed at
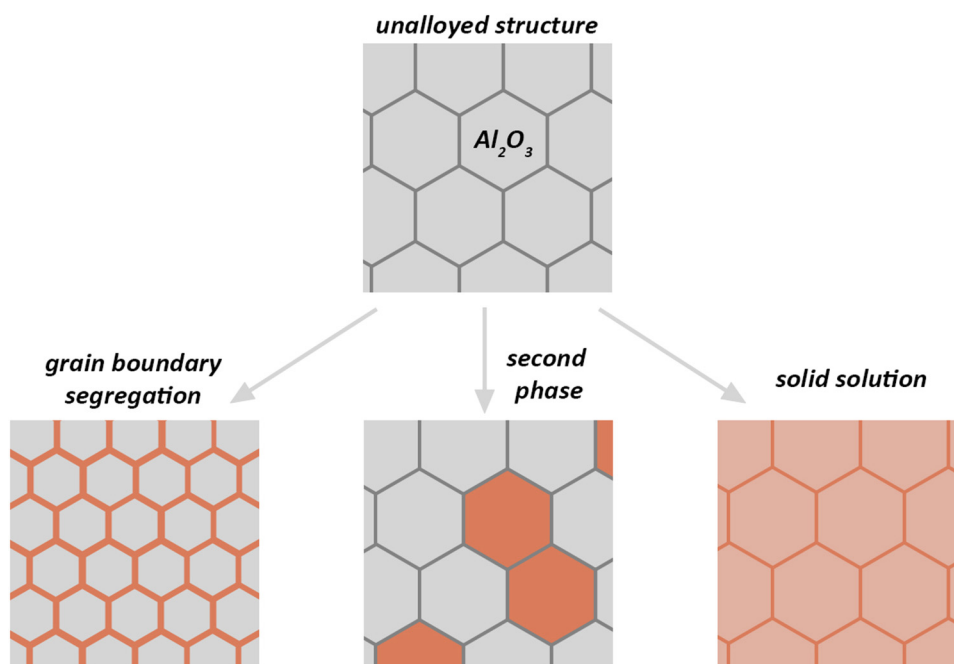

FIG. 23. Schematic illustration of possible impacts of alloying elements within Al_2O_3 thin films: segregation at grain boudaries, formation of a second phase, or formation of a solid solution.
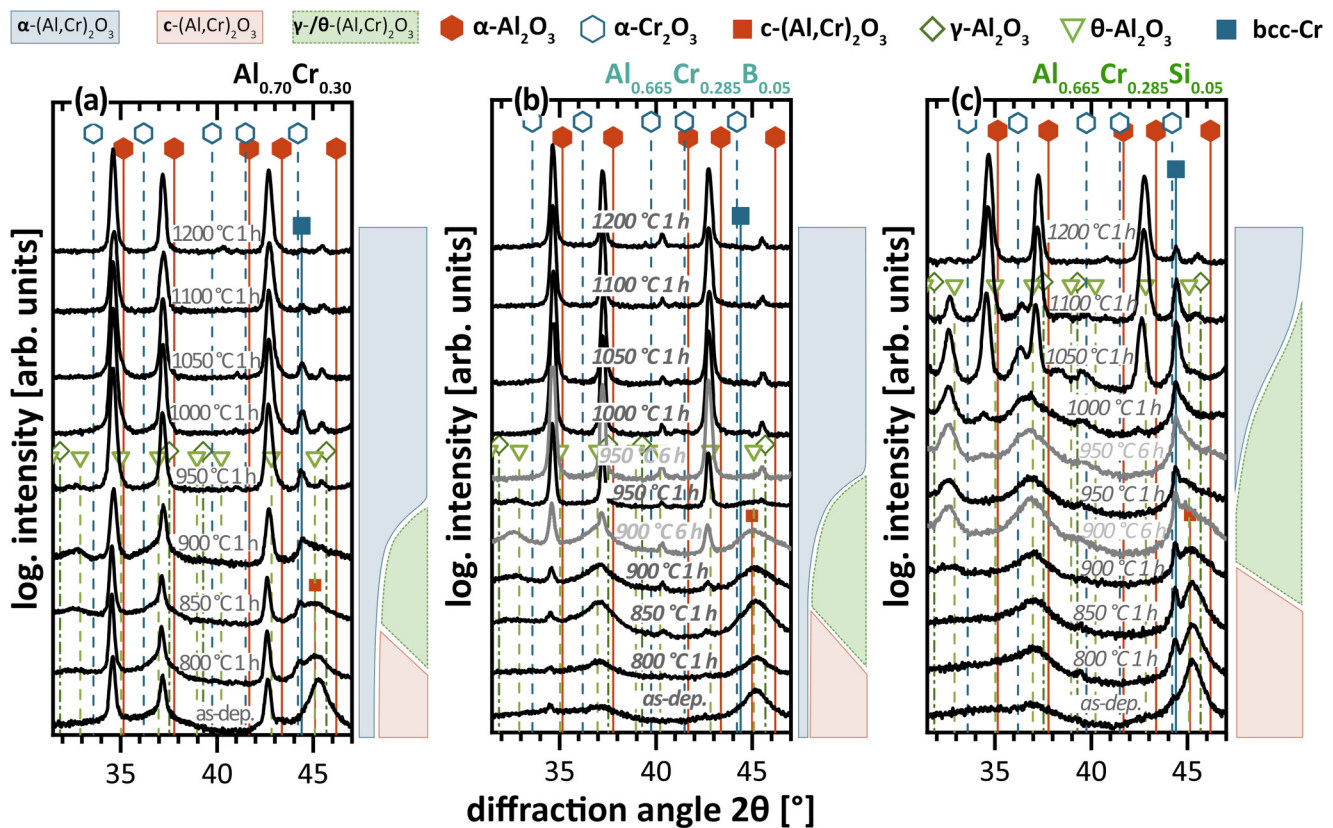
FIG. 24. Powder x-ray diffraction patterns of (a) $Al_{0.70}Cr_{0.30}$-, (b) $Al_{0.665}Al_{0.285}B_{0.05}$-, and (c) $Al_{0.665}Cr_{0.285}Si_{0.05}$-based oxides after vacuum annealing at given temperatures. Adapted from Ref. 67. Reprinted with permission from Koller *et al.*, Surf. Coat. Technol. **342**, 37 (2018). Copyright 2018, Elsevier.

900 and 950 °C for 6 h instead of 1 h). The most noticeable effect on the phase transformation sequence in multiphased $(Al,Cr)_2O_3$ coatings is given for Si additions, see Fig. 24(c). The phase transition from metastable cubic into mixed cubic γ-/θ-type is shifted to 900–1000 °C, and a single-phase hexagonal $(Al,Cr)_2O_3$ solid solution is not observed before annealing at 1100 °C.

Thus, next to the beneficial effect of suppressing the formation of nonconductive oxide pillars at the cathode surface, the phase transition from metastable phases into a corundum-type solid solution can effectively been achieved by small amounts of B or Si.

Next to fully stoichiometric $(Al_{1-x}Cr_x)_2O_3$ coatings, the response of intermetallic and substoichiometric (prepared 50 and 100 sccm O_2 p.a.s.) Al-Cr and Al-Cr-Fe-based films upon postdeposition oxidation was recently investigated in more detail.[116,117]

The intermetallic films primarily oxidize from the surface and—depending on the temperature and oxidation duration—form outermost Al-rich oxide scales (Fig. 25). At lower temperatures, primarily γ- and/or θ-Al_2O_3 structures form. Beyond 1100 °C, the outermost coating surface transforms into the corundum structure, which is in agreement with the oxidation pathways of Al-Cr- or Al-Fe-based bulk materials[90,118,119] and metastable Al_2O_3 coatings.[19,120] The strong XRD peak of intermetallic Al_8Cr_5 phases indicates a larger fraction of unoxidized material underneath the oxide scale even up to $T_{ox} = 1300$ °C.

These findings are corroborated by complementary TEM and STEM investigations.[116]

Contrarily, the coatings prepared with 50 sccm O_2 p.a.s. indicate pure α-Al_2O_3 already after oxidation at 900 °C for 3 h, whereas $(Al_{1-x}Cr_x)_2O_3$ solid solutions could not be detected after any of the annealing conditions. The coating prepared with 100 sccm O_2 shows only weak α-Al_2O_3 XRD peaks at low annealing temperatures but for $T_{ox} = 1100$, 1200, and 1300 °C also $(Al_{1-x}Cr_x)_2O_3$ solid solutions.

These results highlight that the pathways of oxidization of nonstoichiometric $(Al_{1-x}Cr_x)_2O_3$ films strongly depends on the initial microstructure and oxygen content. By alloying (i.e., Fe), the phase formation particularly for the 50 and 100 sccm O_2 p.a.s. coating can further be modified.[116,117]

The evolving microstructures of these substoichiometric coatings can be of high complexity as the examples of the Fe-alloyed coating prepared with 50 sccm O_2 p.a.s. annealed at 1100 °C shows, see Fig. 26. Contrast differences in the STEM image and the corresponding EDS line scan [Figs. 26(b) and 26(c)] reveal chemical fluctuations of Al- and O-rich regions next to almost unoxidized Cr- and Fe-rich domains. This is quite interesting and to some extent resembles the substoichiometric coating regime observed in gradually structured films. Apparently, Al is preferentially oxidized whereas Cr and Fe maintain (inter)metallicity. Only for higher temperatures (consider the miscibility gape in the Al_2O_3–Cr_2O_3 phase diagram[49] and increased driving force for diffusion), solid solutions form.
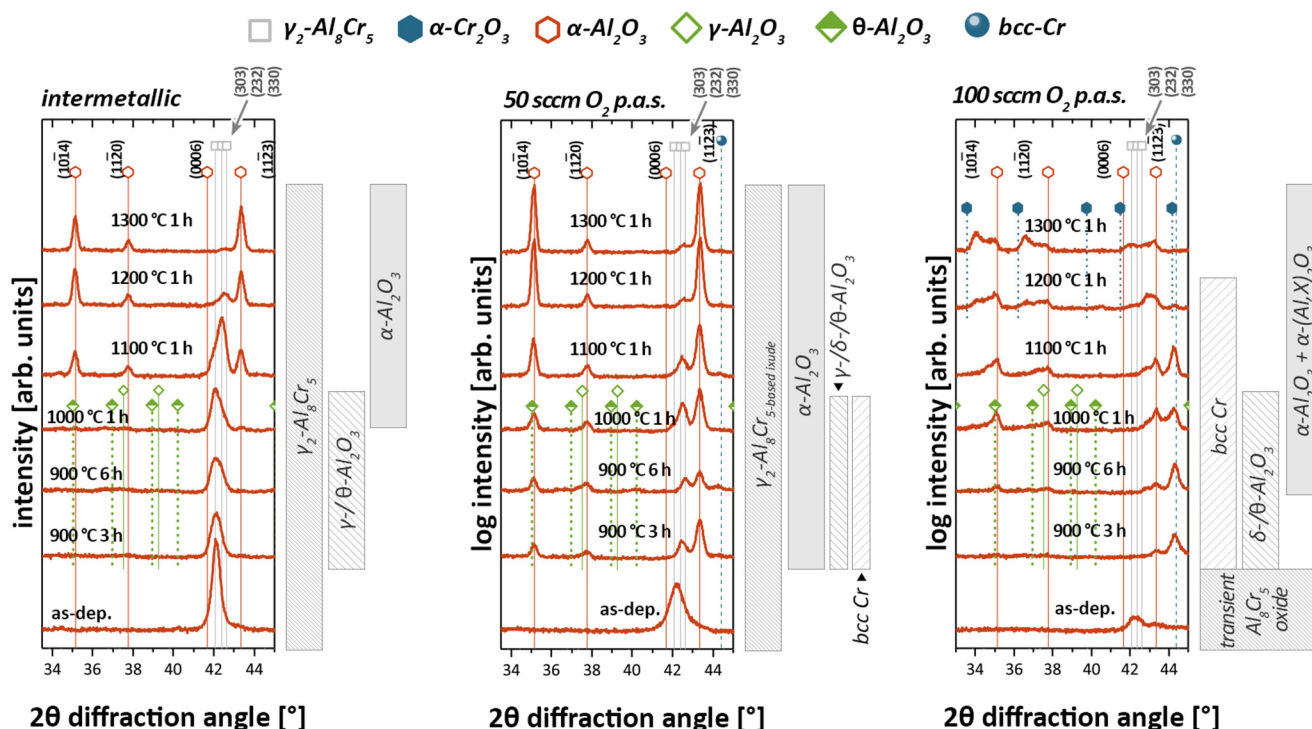
FIG. 25. GID XRD patterns of $Al_{0.70}Cr_{0.30}$-based coatings on sapphire substrates after postdeposition annealing with indicated phase regimes. (a) intermetallic coating and (b) and (c) substoichiometric coatings prepared with 50 and 100 sccm O_2 p.a.s., respectively. Adapted from Ref. 117. Reprinted with permission from Koller et al., J. Vac. Sci. Technol. A 37, 041503. Copyright 2019, American Vacuum Society.

IV. NEW SESQUIOXIDES THIN FILMS AND FURTHER CONCEPTS FOR PROTECTIVE OXIDE PVD COATINGS

Adding to the detailed description of the development of the Al-Cr-based sesquioxide thin films, it has to be mentioned that the quest for advanced protective oxide coatings for engineering applications include further promising concepts for the microstructural design and synthesis of such materials. Advanced alloying strategies [e.g., by incorporating third metals or other elements at lower concentration into the parental $(Al_{1-x}Cr_x)_2O_3$ solid solution] and specific multilayer-based approaches (e.g., special combinations of new oxide layers with traditional transition metal nitrides and similar layers) have been touched in Sec III.

This section addresses briefly other, very recent developments in the field, with a main focus on the PVD synthesis and novel sesquioxide thin films. In consequence, a new research on ZrO_2-based thin films with monoclinic, tetragonal, or cubic structures is not considered in this work (and would be subject of an individual review article itself). We mention here simply that, for example, ZrO_2 and HfO_2 are isostructural materials allowing for a huge variety of single-phase solid solutions of $(Zr_{1-x}Hf_xO_2)$ with very promising properties, especially if phase transformations can be utilized for developing a desired property profile.

Recently, potential novel Cr-based transition metal sesquioxide thin films for protective applications have been reported. Cr_2O_3 is, as already mentioned before, isostructural with Al_2O_3 crystallizing more easily in the corundum structure. However, it exists also in other oxide structures such as CrO_2 or CrO_3—the latter of which is reported volatile at temperature exceeding 1000 °C.[121] Cr_2O_3 can be grown in the corundum structure at less harsh conditions (e.g., at lower synthesis temperatures) compared to Al_2O_3.[37,122]
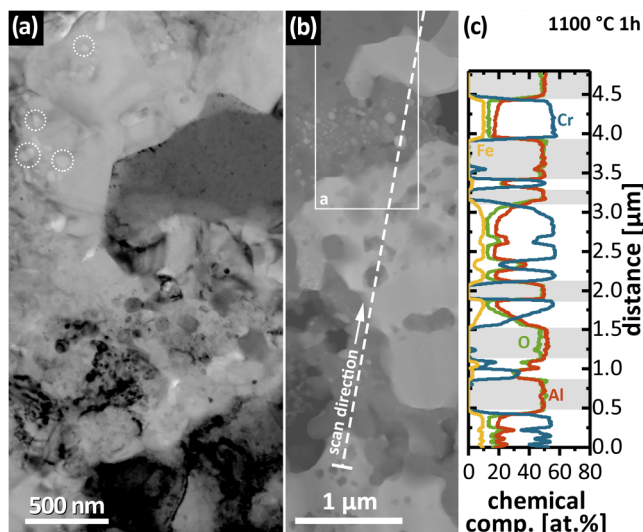
FIG. 26. (a) TEM BF and (b) STEM image with the corresponding EDS line scan shown in (c) of a $Al_{0.675}Cr_{0.275}Fe_{0.05}$-based coating synthesized with 50 sccm O_2 after oxidation at 1100 °C for 1 h. Al-rich areas with M_2O_3 stoichiometry are indicated by a gray shaded background. Adapted from Ref. 116. Reprinted with permission from Koller et al., J. Vac. Sci. Technol. A 37, 041504. Copyright 2019, American Vacuum Society.

Detailed expertize on PVD synthesis of pure Cr_2O_3 thin films has been acquired in the past, see representatively Refs. 37 and 122–125.

Cr_2O_3 is known as a hard material demonstrating also an excellent thermal and chemical stability as well as reasonable mechanical properties[123,126–128]—a combination of utmost interest for various technical applications. Therefore, its combination with other elements forming transition metal sesquioxides can be used to extend the potential of this thin film material.

When looking for potential alloys in Cr_2O_3 thin films, there are at least two essential parameters that can be used to estimate the alloys suitability: the ionic radius of the alloying element and the crystallographic structure of its related oxide.

A. Cr-V-O

One of the transition metals of interest is vanadium. The difference between V^{3+} and Cr^{3+} is with approximately 2.5 p.m. only small,[126] and both oxides crystallize in the corundum structure while V also forms other oxide structures.[129] Interestingly, the equilibrium phase diagram of Cr_2O_3 and V_2O_3, similar to Al_2O_3–Cr_2O_3, exhibits a wide miscibility gap at lower temperatures,[49] which can, by means of PVD methods with its high cooling rates, be overcome and used to realize novel thin films with sophisticated nanoscale structure and atomic arrangement.

Spitz *et al.* have investigated Cr-V-O thin films in a combinatorial approach using a segmented Cr-V target in r.f. reactive magnetron sputtering at moderate substrate temperature of $350\,°C$.[130] The V content within the coatings (and consequently metal-to-oxygen ratio of $^2/_5$ and even $^1/_2$) determines the microstructure. As-deposited Cr-rich films crystallize in a polycrystalline corundum structure, $(Cr,V)_2O_3$, whereas higher V contents lead to amorphous films with distinctively decreased hardness values ($\sim$5 GPa). They additionally found, that, provided $(Cr,V)_2O_3$ crystallize in the corundum structure, small amounts of V effectively increase the hardness, which can even be fortified by applying a substrate bias of -100 V.

Querré *et al.* deposited Cr-V-O coatings by reactive magnetron cosputtering from Cr and V targets without intentional substrate heating. The as-deposited coatings with Cr content up to 60 at. % were x-ray amorphous, while post annealing at $500\,°C$ in defined oxygen containing atmosphere resulted in the crystallization of the films in a single-phase $(V_{1-x}Cr_x)_2O_3$ structure. These films exhibited interesting metal-insulator-transitions, making them promising candidates for memory devices.[131]

The alloying of Cr_2O_3 with V can thus be a promising method to enhance its properties by forming a $(Cr,V)_2O_3$ solid solution and thus opens the possibility for new fields of application for this protective film.

Other metals forming oxides with a Me_2O_3 stoichiometry and offering a structural "compatibility" with Cr_2O_3 (or Al_2O_3) include, for example, Fe, Y, Ga, La, In, or even Mo and W.[132] However, not much work has been published on such alloy thin films with a corundum structure for protective applications. Way more research has been done on such alloys for functional applications, for example, in photocatalytics, optics, and electronics.[133–137] As these topics are out of scope of this work, we mention here exemplarily only a few, relevant, and indicative works. Solid solution thin films of $(Fe_{1-x}Cr_x)_2O_3$ with corundum structure have been reported due to their great potential for bandgap design, enabling potential applications in photocatalysis. These films were grown by pulsed laser deposition (PLD)[133] or molecular beam epitaxy (MBE).[134,135] As V has been discussed as potential alloying element into Cr_2O_3, it should be noted that it has as well been successfully used to synthesize solid solution thin films of $(Fe_{1-x}V_x)_2O_3$ with tuneable electrical conductivity.[137] Even more complex coatings with corundum structure have been reported, such as alloy coatings in the system Ga_2O_3-Cr_2O_3-Fe_2O_3.[138]

B. Cr-Zr-O

Alloying elements forming hard oxides with MeO_2 structure and/or having other valence states than Cr^{3+} include zirconium, hafnium, titanium, or others. Among these, zirconium has been considered as alloying element of large interest with regard of the fact that ZrO_2 is a well-investigated and widely-applied functional oxide material, particularly as thermal barrier coating for, e.g., turbine applications.[139–141] It exists in three different structural modifications: monoclinic (which is the stable phase under standard conditions), tetragonal, and cubic. As previously discussed for Al_2O_3 and $(Al,Cr)_2O_3$ polymorphs, phase transformations of ZrO_2 are associated with volume changes—which, depending on the application, may even be beneficial as several examples show.[142,143]

A combinatorial approach was used to study structure-property relationships of r.f. reactively magnetron sputtered Cr-Zr-O coatings by Spitz and co-workers.[144] The coatings were deposited at substrate temperature of $500\,°C$ onto cemented carbide and Si wafer substrates. A single-phased corundum-type $(Cr,Zr)_2O_3$ solid solution was formed up to Zr contents of 12 at. %. The corresponding metal-to-oxygen ratio Me/O very well reflects the ideal value for sesquioxides of $^2/_3$. By further increasing the Zr content (yet with identical reactive gas pressure as the coatings were prepared by one deposition), however, a cubic $(Zr,Cr)O_2$ solid solution and Me/O-ratios of $\sim^1/_2$ are observed. Even higher Zr contents in the coatings lead to monoclinic and tetragonal structures, and the highest Zr contents lead to multistructured $(Zr,Cr)_2$ films consisting of tetragonal and monoclinic phases. These relations are schematically illustrated in Fig. 27.

Landälv *et al.* investigated the thermal stability of above described Cr-rich $(Cr,Zr)_2O_3$ thin films, deposited now on Ti alloy substrates. They revealed in a detailed TEM investigation that the as-deposited corundum-type films already contained segregation of Cr and Zr at the nanoscale, forming a small fraction of an amorphous $(Zr,Cr)O_x$ phase. The microstructural evolution of these films during vacuum annealing treatments up to $870\,°C$ has been elaborated. Annealing at $750\,°C$ resulted in crystallization of the amorphous phase into a tetragonal ZrO_2 with dissolved Cr. Annealing to $810\,°C$ led to further crystallization of this phase and the
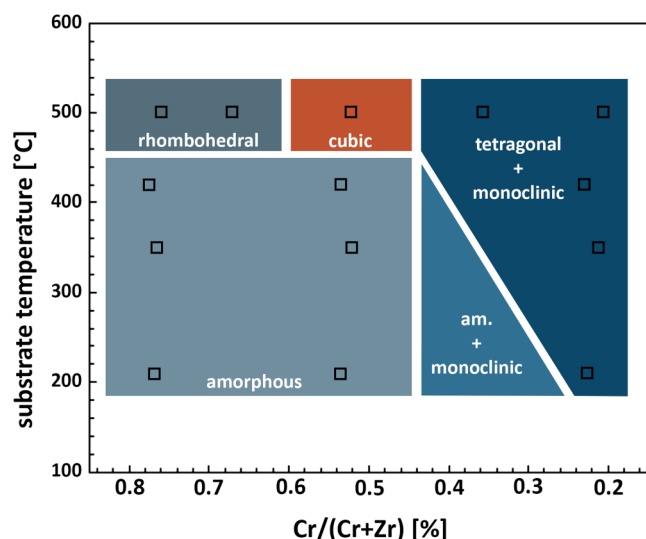
FIG. 27. Schematic phase diagram of Cr-Zr-O thin films as a function of chemistry and deposition temperature. Adapted from Ref. 145.

formation of a crystalline composite of α-$(Cr,Zr)_2O_3$ and t-$(Zr,Cr)O_2$ phases was observed. This change in microstructure was accompanied by a significant increase of the film hardness (so-called age hardening effect). When the films were annealed at 870 °C, a structure composed of tetragonal ZrO_2 and metallic bcc-Cr phases was formed.[146] While the thermal stability of the $(Cr,Zr)_2O_3$ solid solution is obviously much lower than that of a $(Al,Cr)_2O_3$ solid solution, this work contributed to the development of advanced oxide film concepts for wear resistant coatings.

Rafaja *et al.* deposited Cr-Zr-O thin films by reactive ion beam sputtering of Cr-Zr targets without intentional substrate heating. The deposition process led to a substrate temperature below 60 °C, and, in consequence, the as-deposited thin films with Zr content between 3 and 15 at. % were x-ray amorphous. Subsequent annealing up to 1100 °C in *in situ* synchrotron diffraction studies revealed a crystallization behavior of the films that was clearly influenced by the Zr content. The authors demonstrated the preferred crystallization of a hexagonal $(Cr,Zr)_2O_3$ phase for Cr-rich coatings, while the crystallization of a zirconium-rich $(Zr,Cr)O_2$ phase was retarded.

For coatings with a Zr content of 3 at. %, the crystallization of the corundum solid solution phase started at 600 °C. A higher Zr content in the coatings resulted in a shift of the crystallization onset temperature of this phase, while films with Zr content of 15 at. % remained in amorphous state even if annealed up to 1000 °C. According to Rafaja *et al.*, the corundum $(Cr,Zr)_2O_3$ phase should be able to incorporate Zr up to 3 at. %, before segregation from oversaturated solid solution should start and result in the formation of a second ZrO_2-based solid solution, resulting in a two-phase nanocomposite structure. Thus, the work of Rafaja *et al.* is well in accordance with that of Spitz *et al.* and demonstrates that the approach of combined deposition and annealing can be a valuable design tool to obtain advanced protective oxide thin films.[147]

C. Other Cr-based systems

In the area of functional coatings, Pokhrel *et al.* described the synthesis of novel gas sensing thin films by alloying Cr_2O_3 thin films with Ti^{4+} ions in radio frequency sputtering from ceramic targets, resulting in the growth of single-phase $(Cr_{2-x}Ti_x)_2O_3$ thin films on sapphire at 800 °C substrate temperature. The nominal composition of the films was reported to be similar to that of the target, $Cr_{1.8}Ti_{0.2}O_3$.[148]

Noteworthy, the microstructure formation in systems such as Al-Zr-O, Al-Ti-O, or Al-Y-O did not reveal corundum-type thin films in PVD deposition.[149–153] In such systems, different type of oxide nanocomposite thin films have been reported, and the nanocomposite design concept has been proven to be another promising approach toward protective PVD oxide coatings. For example, Trinh *et al.* deposited Al-Zr-O thin films by reactive magnetron sputtering from Al and Zr targets at substrate temperature of 300 °C. Films with Al concentration already above 5 at. % were x-ray amorphous, while Zr-rich films grew in the crystalline form. The authors discussed the impact of Al admixture on the phase formation and growth of zirconia coatings in detail.[153] Another detailed study on Al-Zr-O thin films has been published by Musil *et al.*,[152] who prepared their films by reactive sputtering at 500 °C using ac pulsed dual magnetrons. They reported the significant influence of the Zr/Al concentration ratio and the oxygen partial pressure on the microstructure formation. Simplified, thin films with Zr/Al < 1 were x-ray amorphous again, while films with Zr/Al > 1 were composites of nanocrystalline ZrO_2 and amorphous Al_2O_3 phases. These latter types of coatings exhibited interesting mechanical properties with respect to resistance to cracking. Based on a simulation study by density functional theory, thermodynamic modeling, and comparison of calculated data with other theoretical and experimental work, Sheng *et al.* suggested that the hypothetical ternary solid solutions in this system, hexagonal $(Zr_{1-x}Al_x)_2O_3$ and monoclinic $(Zr_{1-x}Al_x)O_2$, should undergo immediate spinodal decomposition in the parameter range usually applied in plasma-assisted PVD, leading to the formation of nanocomposite coatings of Al_2O_3/ZrO_2 with potentially enhanced properties in comparison to the solid solutions.[151] This nanocomposite design concept is another promising tool to develop protective oxide thin films with enhanced properties.[154]

V. CONCLUSION AND OUTLOOK

The continuous and steadily growing industrial interested in enhanced protective coating materials has also affected Al-based oxides. Yet, despite other thin film materials systems such as nitrides, the inherent nature of oxides implies certain challenges in the deposition process. From an applicational point of view, the major demand is the ability to synthesize crystalline coatings at reduced growth temperatures in order to make temperature-sensitive substrate materials accessible. The ideal structure would be a corundum-type solid solution with an Al-content as high as possible. However, the higher the Al-content, the more

likely are dual-phased compositions containing metastable phase fractions. These, depending whether further alloying elements are present, tend to transform into the corundum structure at elevated temperatures (referring to the here shown examples of B and Si between 800 and 950 °C) and thus give rise to crack generation as a result of volume changes. The most effective way to synthesize α-structured $(Al_{1-x}Cr_x)_2O_3$ thin films is the use of Cr-rich cathodes and alloying concepts including Fe are only partially successfully. Also changed growth conditions like higher O_2 partial pressure values or increased substrate biasing does not lead to a real breakthrough in synthesizing $(Al_{1-x}Cr_x)_2$-O_3 thin films entirely in the α-structure. The only concept that was yet successful is based on Cr_2O_3 or $(Cr,Al)_2O_3$ seed or multilayers.

The second approach in the synthesis of $(Al,Cr)_2O_3$-based coatings by cathodic arc evaporation is the alloying with elements that, although supressing the α phase, are capable of retarding the thermally-induced phase transition sequence. These are, for instance, B or Si, both of which also seem to beneficially influence the formation of nonconductive oxide pillars on the cathode surface during O_2 containing evaporation processes.

We can clearly state that the cathodic arc evaporation of $(Al,Cr)_2O_3$-based coatings is everything but straightforward and to entirely understand the synthesis and growth process, all aspects of the deposition—beginning with the cathode microstructure and ending by the anticipated conditions during application—must be considered/taken into consideration. A significant progress in all these fields could be achieved by various research groups and potentially new applications are already being evaluated.

Furthermore, the examples of V and Zr-alloyed Cr_2O_3 coatings demonstrate that the capability of Chromia synthesized by PVD methods is by far yet not exploited. Novel design or alloying concepts are still to be investigated, opening a broad field of potential applications based on enhanced mechanical, chemical, or electrical properties.

ACKNOWLEDGMENTS

[1]J. E. Greene, Appl. Phys. Rev. **1**, 041302 (2014).

[2]T. I. Selinder, E. Coronel, E. Wallin, and U. Helmersson, Int. J. Refract. Met. Hard Mater. **27**, 507 (2009).

[3]E. Serra, G. Benamati, and O. V Ogorodnikova, J. Nucl. Mater. **255**, 105 (1998).

[4]I. Levin and D. Brandon, J. Am. Ceram. Soc. **81**, 1995 (1998).

[5]J. M. Schneider, W. D. Sproul, and A. Matthews, Surf. Coat. Technol. **98**, 1473 (1998).

[6]M. S. Jochen, D. S. William, and M. Allan, Surf. Coat. Technol. **94–95**, 179 (1997).

[7]O. Zywitzki and G. Hoetzsch, Surf. Coat. Technol. **94–95**, 303 (1997).

[8]O. Zywitzki and G. Hoetzsch, Surf. Coat. Technol. **86–87**, 640 (1996).

[9]J. M. Andersson, "Controlling the formation and stability of alumina phases," Ph.D. thesis (Linköping University, The Institute of Technology, 2005).

[10]S. Ruppi, A. Larsson, and A. Flink, Thin Solid Films **516**, 5959 (2008).

[11]K. Wefers and C. Misra, Alcoa Research Laboratories Technical Paper No. 19, 1987.

[12]S. Ruppi, Int. J. Refract. Met. Hard Mater. **23**, 306 (2005).

[13]M. Åstrand, T. I. Selinder, F. Fietzke, and H. Klostermann, Surf. Coat. Technol. **188–189**, 186 (2004).

[14]F. Klocke, K. Gerschwiler, R. Fritsch, and D. Lung, Surf. Coat. Technol. **201**, 4389 (2006).

[15]S. E. Cordes, CIRP J. Manuf. Sci. Technol. **5**, 20 (2012).

[16]S. Ruppi and A. Larsson, Thin Solid Films **388**, 50 (2001).

[17]D. H. Trinh, K. Back, G. Pozina, H. Blomqvist, T. Selinder, M. Collin, I. Reineck, L. Hultman, and H. Högberg, Surf. Coat. Technol. **203**, 1682 (2009).

[18]P. Eklund, M. Sridharan, G. Singh, and J. Bøttiger, Plasma Process. Polym. **6**, S907 (2009).

[19]V. Edlmayr, T. P. Harzer, R. Hoffmann, D. Kiener, C. Scheu, and C. Mitterer, J. Vac. Sci. Technol. A **29**, 041506 (2011).

[20]V. Edlmayr, M. Moser, C. Walter, and C. Mitterer, Surf. Coat. Technol. **204**, 1576 (2010).

[21]I. Levin, L. A. Bendersky, D. G. Brandon, and M. Rühle, Acta Mater. **45**, 3659 (1997).

[22]C. Wolverton and K. Hass, Phys. Rev. B **63**, 024102 (2000).

[23]J. M. McHale, Science (80-) **277**, 788 (1997).

[24]R. Brill, F. Koch, J. Mazurelle, D. Levchuk, M. Balden, Y. Yamada-Takamura, H. Maier, and H. Bolt, Surf. Coat. Technol. **174–175**, 606 (2003).

[25]H. G. Prengel, W. Heinrich, G. Roder, and K. H. Wendt, Surf. Coat. Technol. **68–69**, 217 (1994).

[26]R. Snyders, K. Jiang, D. Music, S. Konstantinidis, T. Markus, A. Reinholdt, J. Mayer, and J. M. Schneider, Surf. Coat. Technol. **204**, 215 (2009).

[27]Y. Yamada-Takamura, F. Koch, H. Maier, and H. Bolt, Surf. Coat. Technol. **142–144**, 260 (2001).

[28]E. Wallin, T. I. Selinder, M. Elfwing, and U. Helmersson, Europhys. Lett. **82**, 36002 (2008).

[29]J. M. Andersson, E. Wallin, U. Helmersson, U. Kreissig, and E. P. Münger, Thin Solid Films **513**, 57 (2006).

[30]J. M. Schneider, K. Larsson, J. Lu, E. Olsson, and B. Hjörvarsson, Appl. Phys. Lett. **80**, 1144 (2002).

[31]J. Houska, Surf. Coat. Technol. **254**, 131 (2014).

[32]J. Houska, Surf. Coat. Technol. **235**, 333 (2013).

[33]P. Jin, S. Nakao, S. X. Wang, and L. M. Wang, Appl. Phys. Lett. **82**, 1024 (2003).

[34]P. Jin, G. Xu, M. Tazawa, K. Yoshimura, D. Music, J. Alami, and U. Helmersson, J. Vac. Sci. Technol. A **20**, 2134 (2002).

[35]T. Kohara, H. Tamagaki, Y. Ikari, and H. Fujii, Surf. Coat. Technol. **185**, 166 (2004).

[36]K. Dumbuya, K. Christmann, and S. L. M. Schroeder, Langmuir **23**, 5386 (2007).

[37]Y. Gao, H. Leiste, M. Stueber, and S. Ulrich, J. Cryst. Growth **457**, 158 (2017).

[38]Y. Gao, H. Leiste, S. Ulrich, and M. Stueber, Thin Solid Films **644**, 129 (2017).

[39]M. Bartosik, R. Hahn, M. Arndt, P. Polcik, and P. H. Mayrhofer, presented at the 19th Plansee Seminar 2017, Vol. 72, p. 1.

[40]R. Hahn, M. Bartosik, R. Soler, C. Kirchlechner, G. Dehm, and P. H. Mayrhofer, Scr. Mater. **124**, 67 (2016).

[41]R. Cremer, M. Witthaut, D. Neuschütz, G. Erkens, T. Leyendecker, and M. Feldhege, Surf. Coat. Technol. **120–121**, 213 (1999).

[42]H. Bolvardi, M. to Baben, F. Nahif, D. Music, V. Schnabel, K. P. Shaha, S. Mráz, J. Bednarcik, J. Michalikova, and J. M. Schneider, J. Appl. Phys. **117**, 025302 (2015).

[43]F. Nahif, D. Music, S. Mráz, H. Bolvardi, L. Conrads, and J. M. Schneider, Surf. Coat. Technol. **235**, 250 (2013).

[44]J. M. Andersson, E. Wallin, V. Chirita, E. P. Münger, and U. Helmersson, Phys. Rev. B **71**, 014101 (2005).

[45]E. Wallin, J. M. Andersson, V. Chirita, and U. Helmersson, J. Phys. Condens. Matter **16**, 8971 (2004).

[46]Y.-R. Luo, *Comprehensive Handbook of Chemical Bond Energies* (CRC, Boca Raton, FL, 2007).

[47]D. E. Ashenford, F. Long, W. E. Hagston, B. Lunn, and A. Matthews, Surf. Coat. Technol. **119**, 699 (1999).

[48]M. Ristić, S. Popović, and S. Musić, Mater. Lett. **16**, 309 (1993).

[49]S. S. Kim and T. H. Sanders, J. Am. Ceram. Soc. **84**, 1881 (2001).

[50]G. Rollmann, A. Rohrbach, P. Entel, and J. Hafner, Phys. Rev. B Condens. Matter Mater. Phys. **69**, 165107 (2004).

[51]H. Holleck, Surf. Coat. Technol. **36**, 151 (1988).

[52]H. W. Holleck, Vacuum **41**, 2220 (1990).

[53]D. Hochauer, C. Mitterer, M. Penoy, C. Michotte, H. P. Martinz, and M. Kathrein, Surf. Coat. Technol. **204**, 3713 (2010).

[54]J. Ramm, A. Neels, B. Widrig, M. Döbeli, L. de A. Vieira, A. Dommann, and H. Rudigier, Surf. Coat. Technol. **205**, 1356 (2010).

[55]M. Pohler, R. Franz, J. Ramm, P. Polcik, and C. Mitterer, Surf. Coat. Technol. **206**, 1454 (2011).

[56]J. Ramm, M. Ante, T. Bachmann, B. Widrig, H. Brändle, and M. Döbeli, Surf. Coat. Technol. **202**, 876 (2007).

[57]M. Witthaut, R. Cremer, K. Reichert, and D. Neuschütz, Microchim. Acta **133**, 191 (2000).

[58]D. Diechle, M. Stueber, H. Leiste, S. Ulrich, and V. Schier, Surf. Coat. Technol. **204**, 3258 (2010).

[59]D. Diechle, *Herstellung Und Charakterisierung Oxidbasierter PVD-Hartstoffschichten in Den Stoffsystemen Al-Cr-O Und Al-Cr-O-N* (Karlsruhe Institut für Technologie, Karlsruhe, 2012).

[60]V. Edlmayr, M. Pohler, I. Letofsky-Papst, and C. Mitterer, Thin Solid Films **534**, 373 (2013).

[61]M. Pohler, R. Franz, J. Ramm, P. Polcik, and C. Mitterer, Surf. Coat. Technol. **282**, 43 (2015).

[62]J. Ramm, M. Ante, H. Brändle, A. Neels, A. Dommann, and M. Döbeli, Adv. Eng. Mater. **9**, 604 (2007).

[63]H. Najafi, A. Karimi, P. Dessarzin, and M. Morstein, Surf. Coat. Technol. **214**, 46 (2013).

[64]D. Levchuk, H. Bolt, M. Döbeli, S. Eggenberger, B. Widrig, and J. Ramm, Surf. Coat. Technol. **202**, 5043 (2008).

[65]L. de Abreu Vieira, M. Döbeli, A. Dommann, E. Kalchbrenner, A. Neels, J. Ramm, H. Rudigier, J. Thomas, and B. Widrig, Surf. Coat. Technol. **204**, 1722 (2010).

[66]V. Dalbauer, J. Ramm, S. Kolozsvári, V. Paneta, C. M. Koller, and P. H. Mayrhofer, Surf. Coat. Technol. **352**, 392 (2018).

[67]C. M. Koller, V. Dalbauer, A. Schmelz, R. Raab, P. Polcik, J. Ramm, and P. H. Mayrhofer, Surf. Coat. Technol. **342**, 37 (2018).

[68]H. Okamoto, J. Phase Equilib. Diffus. **29**, 112 (2008).

[69]C. M. Koller, J. Ramm, S. Kolozsvári, F. Munnik, J. Paulitsch, and P. H. Mayrhofer, Scr. Mater. **97**, 49 (2015).

[70]A. Khatibi, J. Palisaitis, C. Höglund, A. Eriksson, POÅ Persson, J. Jensen, J. Birch, P. Eklund, and L. Hultman, Thin Solid Films **519**, 2426 (2011).

[71]M. Hans *et al.*, Surf. Coat. Technol. **305**, 249 (2016).

[72]C. M. Koller, V. Dalbauer, A. Kirnbauer, S. Löffler, S. Kolozsvári, J. Ramm, and P. H. Mayrhofer, Scr. Mater. **139**, 144 (2017).

[73]V. Dalbauer, J. Ramm, S. Kolozsvári, C. M. Koller, and P. H. Mayrhofer, Thin Solid Films **87**, 1 (2017).

[74]C. M. Koller, V. Dalbauer, S. Kolozsvári, J. Ramm, and P. H. Mayrhofer, Vacuum **155**, 645 (2018).

[75]L. Vegard, Z. Phys. **5**, 17 (1921).

[76]B. B. B. Alling, A. Khatibi, S. I. Simak, P. Eklund, and L. Hultman, J. Vac. Sci. Technol. A **31**, 030602 (2013).

[77]R. Franz, F. Mendez Martin, G. Hawranek, and P. Polcik, J. Vac. Sci. Technol. A **34**, 021304 (2016).

[78]C. M. Koller, R. Hahn, J. Ramm, S. Kolozsvári, and P. H. Mayrhofer, J. Vac. Sci. Technol. A **34**, 021603 (2016).

[79]R. Franz, J. Wallig, P. Polcik, and A. Anders, *Proceedings—International Symposium on Discharges and Electrical Insulation in Vacuum, ISDEIV*, Tomsk, Russia, 2–7 September 2012 (IEEE, New York, 2012), p. 541.

[80]R. Franz, P. Polcik, and A. Anders, IEEE Trans. Plasma Sci. **41**, 1929 (2013).

[81]A. Anders, Surf. Coat. Technol. **121**, 319 (1999).

[82]H. Bolt, F. Koch, J. L. Rodet, D. Karpov, and S. Menzel, Surf. Coat. Technol. **116–119**, 956 (1999).

[83]J. Paulitsch, R. Rachbauer, J. Ramm, P. Polcik, and P. H. Mayrhofer, Vacuum **100**, 29 (2014).

[84]C. M. Koller, V. Dalbauer, A. Kirnbauer, M. Sauer, S. Kolozsvári, J. Ramm, and P. H. Mayrhofer, Scr. Mater. **152**, 107 (2018).

[85]K. Jiang, D. Music, K. Sarakinos, and J. M. Schneider, J. Phys. Condens. Matter **22**, 505502 (2010).

[86]D. Music, F. Nahif, K. Sarakinos, N. Friederichsen, and J. M. Schneider, Appl. Phys. Lett. **98**, 111908 (2011).

[87]C. M. Koller, N. Koutná, J. Ramm, S. Kolozsvári, J. Paulitsch, D. Holec, and P. H. Mayrhofer, AIP Adv. **6**, 025002 (2016).

[88]D. Holec, L. Zhou, H. Riedl, C. M. Koller, P. H. Mayrhofer, M. Friák, M. Šob, F. Körmann, J. Neugebauer, D. Music, M. A. Hartmann, and F. D. Fischer, Adv. Eng. Mater. **19**, 1600688 (2017).

[89]A. H. Schultz and V. S. Stubican, J. Am. Ceram. Soc. **53**, 613 (1970).

[90]X. F. Zhang, K. Thaidigsmann, J. Ager, and P. Y. Hou, J. Mater. Res. **21**, 1409 (2006).

[91]E. Airiskallio, E. Nurmi, M. H. Heinonen, I. J. Väyrynen, K. Kokko, M. Ropo, M. P. J. Punkkinen, H. Pitkänen, M. Alatalo, J. Kollár, B. Johansson, and L. Vitos, Corros. Sci. **52**, 3394 (2010).

[92]M. Mühlbacher, R. Franz, J. Paulitsch, H. Rudigier, P. Polcik, P. H. Mayrhofer, and C. Mitterer, Surf. Coat. Technol. **215**, 96 (2013).

[93]C. M. Koller, J. Ramm, S. Kolozsvári, J. Paulitsch, and P. H. Mayrhofer, Surf. Coat. Technol. **276**, 735 (2015).

[94]C. M. Koller, R. Hahn, B. Widrig, J. Ramm, S. Kolozsvári, J. Paulitsch, and P. H. Mayrhofer, BHM Berg- Hüttenmänn. Monatsh. **161**, 325 (2016).

[95]J. A. Thornton, Thin Solid Films **107**, 3 (1983).

[96]R. Hollerweger, L. Zhou, D. Holec, C. M. Koller, R. Rachbauer, P. Polcik, and P. H. Mayrhofer, J. Appl. Phys. **119**, 065304 (2016).

[97]C. Sabitzer, J. Paulitsch, S. Kolozsvári, R. Rachbauer, and P. H. Mayrhofer, Vacuum **106**, 49 (2014).

[98]J. Lin, J. J. Moore, W. D. Sproul, S. L. Lee, and J. Wang, IEEE Trans. Plasma Sci. **38**, 3071 (2010).

[99]I. Petrov, L. Hultman, J.-E. Sundgren, and J. E. Greene, J. Vac. Sci. Technol. A **10**, 265 (1992).

[100]J. Rosén, S. Mráz, U. Kreissig, D. Music, and J. M. Schneider, Plasma Chem. Plasma Process. **25**, 303 (2005).

[101]A. D. Pogrebnjak, O. V. Bondar, S. O. Borba, G. Abadias, P. Konarski, S. V. Plotnikov, V. M. Beresnev, L. G. Kassenova, and P. Drodziel, Nucl. Instrum. Methods Phys. Res. B **385**, 74 (2016).

[102]G. Abadias, E. Chason, J. Keckes, M. Sebastiani, G. B. Thompson, E. Barthel, G. L. Doll, C. E. Murray, C. H. Stoessel, and L. Martinu, J. Vac. Sci. Technol. A **36**, 020801 (2018).

[103]C. M. Koller, S. A. Glatz, S. Kolozsvári, J. Ramm, and P. H. Mayrhofer, Surf. Coat. Technol. **319**, 386 (2017).

[104]S. Ruppi, Surf. Coat. Technol. **202**, 4257 (2008).

[105]J. Vetter, Surf. Coat. Technol. **257**, 213 (2014).

[106]J. M. Andersson, Z. Czigány, P. Jin, and U. Helmersson, J. Vac. Sci. Technol. A **22**, 117 (2004).

[107]P. Eklund, M. Sridharan, M. Sillassen, and J. Bøttiger, Thin Solid Films **516**, 7447 (2008).

[108]J. Sun, T. Stirner, and A. Matthews, Surf. Coat. Technol. **201**, 4205 (2006).

[109]M. Pohler, R. Franz, J. Ramm, P. Polcik, and C. Mitterer, Thin Solid Films **550**, 95 (2014).

[110]C. M. Koller, A. Kirnbauer, S. Kolozsvári, J. Ramm, and P. H. Mayrhofer, Scr. Mater. **146**, 208 (2018).

[111]R. Raab, C. M. Koller, S. Kolozsvári, J. Ramm, and P. H. Mayrhofer, Surf. Coat. Technol. **352**, 213 (2018).

[112]M. Stueber, D. Diechle, H. Leiste, and S. Ulrich, Thin Solid Films **519**, 4025 (2011).

[113]P. H. Mayrhofer, F. D. Fischer, H. J. Böhm, C. Mitterer, and J. M. Schneider, Acta Mater. **55**, 1441 (2007).

[114]R. Rachbauer, E. Stergar, S. Massl, M. Moser, and P. H. Mayrhofer, Scr. Mater. **61**, 725 (2009).

[115]S. Vuorinen and L. Karlsson, Thin Solid Films **214**, 132 (1992).

[116]C. M. Koller, A. Kirnbauer, S. Kolozsvári, J. Ramm, and P. H. Mayrhofer, J. Vac. Sci. Technol. A **37**, 041504 (2019).

[117]C. M. Koller, A. Kirnbauer, V. Dalbauer, S. Kolozsvári, J. Ramm, and P. H. Mayrhofer, J. Vac. Sci. Technol. A **37**, 041503 (2019).

[118]F. H. Stott, G. C. Wood, and J. Stringer, Oxid. Met. **44**, 113 (1995).

[119]J. Engkvist, S. Canovic, F. Liu, H. Götlind, J. E. Svensson, L. G. Johansson, M. Olsson, and M. Halvarsson, Mater. High Temp. **26**, 199 (2009).

[120]A. Larsson, M. Halvarsson, and S. Vuorinen, Int. J. Refract. Met. Hard Mater. **16**, 369 (1998).

[121]H. C. Graham and H. H. Davis, J. Am. Ceram. Soc. **54**, 89 (1971).

[122]K. Pedersen, J. Bøttiger, M. Sridharan, M. Sillassen, and P. Eklund, Thin Solid Films **518**, 4294 (2010).

[123]P. Hones, M. Diserens, and F. Lévy, Surf. Coat. Technol. **120–121**, 277 (1999).

[124]H. C. Barshilia and K. S. Rajam, Appl. Surf. Sci. **255**, 2925 (2008).

[125]J. Lin and W. D. Sproul, Surf. Coat. Technol. **276**, 70 (2015).

[126]R. D. Shannon and C. T. Prewitt, Acta Crystallogr. Sect. B Struct. Crystallogr. Cryst. Chem. **26**, 1046 (1970).

[127]T.-G. Wang, D. Jeong, Y. Liu, Q. Wang, S. Iyengar, S. Melin, and K. H. Kim, Surf. Coat. Technol. **206**, 2638 (2012).

[128]J. Wei and Q. Xue, Wear **199**, 157 (1996).

[129]G. Andersson, J. Paju, W. Lang, and W. Berndt, Acta Chem. Scand. **8**, 1599 (1954).

[130]S. Spitz, M. Stüber, H. Leiste, S. Ulrich, and H. J. Seifert, Surf. Coat. Technol. **257**, 355 (2014).

[131]M. Querré et al., Thin Solid Films **617**, 56 (2016).

[132]N. Becker, C. Reimann, D. Weber, T. Lüdtke, M. Lerch, T. Bredow, and R. Dronskowski, Z. Krist. Cryst. Mater. **232**, 2018 (2017).

[133]H. Mashiko, T. Oshima, and A. Ohtomo, Appl. Phys. Lett. **99**, 97 (2011).

[134]S. E. Chamberlin, Y. Wang, K. Lopata, T. C. Kaspar, A. W. Cohn, D. R. Gamelin, N. Govind, P. V. Sushko, and S. A. Chambers, J. Phys. Condens. Matter **25**, 392002 (2013).

[135]T. C. Kaspar, S. E. Chamberlin, M. E. Bowden, R. Colby, V. Shutthanandan, S. Manandhar, Y. Wang, P. V. Sushko, and S. A. Chambers, J. Phys. Condens. Matter **26**, 135005 (2014).

[136]S. Fujita and K. Kaneko, J. Cryst. Growth **401**, 588 (2014).

[137]S. E. Chamberlin, I. H. Nayyar, T. C. Kaspar, P. V. Sushko, and S. A. Chambers, Appl. Phys. Lett. **106**, 041905 (2015).

[138]K. Kaneko, T. Nomura, and S. Fujita, Phys. Status Solidi Curr. Top. Solid State Phys. **7**, 2467 (2010).

[139]G. McDonald and R. C. Hendricks, Thin Solid Films **73**, 491 (1980).

[140]R. A. Miller, Surf. Coat. Technol. **30**, 1 (1987).

[141]U. Schulz and M. Schmücker, Mater. Sci. Eng. A **276**, 1 (2000).

[142]R. H. J. Hannink, P. M. Kelly, and B. C. Muddle, J. Am. Ceram. Soc. **83**, 461 (2004).

[143]M. Schlögl, C. Kirchlechner, J. Paulitsch, J. Keckes, and P. H. Mayrhofer, Scr. Mater. **68**, 917 (2013).

[144]S. Spitz, M. Stueber, H. Leiste, S. Ulrich, and H. J. Seifert, Thin Solid Films **548**, 143 (2013).

[145]D. Der Ingenieurwissenschaften, "Aufbau und Eigenschaften von PVD-Hartstoffschichten in den Systemen Cr-Zr-O und Cr-Zr-ON," Ph.D. thesis (Karlsruhe Institut für Technologie, Karlsruhe, 2016).

[146]L. Landälv et al., Acta Mater. **131**, 543 (2017).

[147]D. Rafaja, C. Wüstefeld, G. Abrasonis, S. Braeunig, C. Baehtz, F. Hanzig, M. Dopita, M. Krause, and S. Gemming, Thin Solid Films **612**, 430 (2016).

[148]S. Pokhrel, L. Huo, H. Zhao, and S. Gao, Thin Solid Films **516**, 3332 (2008).

[149]F. Nahif, S. Mráz, D. Music, P. Keuter, and J. M. Schneider, Surf. Coat. Technol. **257**, 333 (2014).

[150]J. Musil, V. Šatava, R. Čerstvý, P. Zeman, and T. Tölg, Surf. Coat. Technol. **202**, 6064 (2008).

[151]S. H. Sheng, R. F. Zhang, and S. Veprek, Acta Mater. **59**, 3498 (2011).

[152]J. Musil, J. Sklenka, R. Čerstvý, T. Suzuki, T. Mori, and M. Takahashi, Surf. Coat. Technol. **207**, 355 (2012).

[153]D. H. Trinh, T. Kubart, T. Nyberg, M. Ottosson, L. Hultman, and H. Högberg, Thin Solid Films **516**, 8352 (2008).

[154]J. Musil and P. Baroch, Vacuum **87**, 96 (2013).